APPLICATION OF A THREE-DIMENSIONAL MODEL TO DEEP-WATER WAVE BREAKING

By

JENNIFER L. REGIS

A THESIS PRESENTED TO THE GRADUATE SCHOOL
OF THE UNIVERSITY OF FLORIDA IN PARTIAL FULFILLMENT
OF THE REQUIREMENTS FOR THE DEGREE OF
MASTER OF SCIENCE

UNIVERSITY OF FLORIDA

2005

This work is dedicated to my family.

ACKNOWLEDGMENTS

First and foremost, I wish to thank my immediate family, especially my parents, for their infinite dedication and encouragement. I attribute my accomplishments to date to their love and support, and I thank them for sharing in both my victories as well as my defeats, and for always keeping me laughing. A special acknowledgment goes to my mom, whose courage and strength this past year has reminded me what life is all about. My extended family and friends also deserve recognition for the role each of them took in my social and academic development. Many special thanks are offered to Lieutenant Christopher Steele, for his unwavering belief in my abilities, and for his time, support and inexhaustible ability to make me smile, for which I am eternally grateful.

Credit is due Dr. Donald Slinn, my academic adviser, for his encouragement, ideas, and advice. I would like to extend my gratitude to Drs. Robert Thieke and Andrew Kennedy, of the University of Florida, for the support and guidance they provided as members of my supervisory committee. The remainder of the faculty and staff at the University of Florida, all of whom have made valuable contributions to my experiences the past two years, also deserve many thanks. For their significant contributions to my overall success and happiness in the Civil and Coastal Engineering Department, my office-mates deserve much credit. I would like to give a special thanks to Bret Webb, to whose encouragement, patience, and thoughtfulness I am forever indebted.

Financial assistance for this work was provided by the Office of Naval Research as well as the University of Florida. In addition, funding for much of this research, as well as my education, was administered by the American Society for Engineering

Education (ASEE) in the form of a National Defense Science and Engineering (NDSEG) Fellowship, and I am truly grateful for their consideration.

TABLE OF CONTENTS

LIST OF TABLES

LIST OF FIGURES

Abstract of Thesis Presented to the Graduate School
of the University of Florida in Partial Fulfillment of the
Requirements for the Degree of Master of Science

APPLICATION OF A THREE-DIMENSIONAL MODEL TO DEEP-WATER WAVE BREAKING

By

Jennifer L. Regis

August 2005

Chair: Donald N. Slinn
Major Department: Civil and Coastal Engineering

The complex dynamics associated with deep-water wave breaking events are crucial to the delicate balance between air and sea. The wave breaking process is the chief means by which gases are exchanged across the air-sea interface, as well as the key mechanism by which momentum is imparted into the water column from wind. As such, breaking waves are the driving forces behind such phenomena as ocean circulation, Earth's weather and climate, and global warming trends. Dynamical loadings on ships and offshore structures attributed to the breaking of deep-water waves have been an area of concern for all who travel, build, and live about the sea. Since the pioneering days of Longuet-Higgins, Van Dorn, and Chu in the 1970s, much progress has been made in the study of this important process. Still, the highly nonlinear nature of deep-water breaking waves makes laboratory investigations into the details of this process difficult.

More recently, analysis of deep-water breaking events by means of numerical modeling has become more accessible. Still, this method of investigation is relatively new, and the majority of these studies involve 2D models, of which many only

effectively capture breaking details up to the point of overturning before becoming unstable. In addition, agreement as to the most effective means by which to address such concerns as free-surface and boundary conditions is lacking. Advances in 3D numerical modeling have led to codes that are reasonably well adept at capturing the breaking of shallow-water waves shoaling over a varying bed topography, but have yet, to our knowledge, to be successfully applied to deep-water breaking regimes.

This study involves the modification of a fully 3D, volume of fluid model, entitled TRUCHAS, and the validation of its application to deep-water breaking wave events. Improved capabilities inherent in this model include the capacity to simulate flow dynamics in both fluids, air and water, up to, during, and post-breaking. Our numerical investigation has its basis in laboratory experiments conducted by our partners Mark Donelan and Brian Haus at the Center for Air-Sea Interaction at the University of Miami, in which a focused deep-water wave packet was generated and allowed to evolve to breaking in the Air-Sea Interaction Salt-Water Tank (ASIST). Verification of our numerical model is attempted by means of comparison of model results with those measured in the laboratory. It is our hope that this study serves as a valuable component in the ongoing investigation into this highly variable and dynamic process.

CHAPTER 1
INTRODUCTION

1.1 Background

Over seventy percent of the Earth's surface is covered by water. Mankind has lived on and around great bodies of water for most of its existence, yet remarkably little is understood of the dynamic and complex ways in which the oceans behave. The most vivid example of wave motion and ocean complexity is the sea's capacity to overturn, or break. In particular, deep-water wave breaking is one of the most spectacular events that the sea has to offer, and consequently one of the most perplexing. For ages mankind has struggled to gain the understanding needed to quantify such an energetic and important ocean process.

The breaking of water waves, be it small scale or large, is a vital component of air-sea interaction. Turbulence generated through the breaking process is the dominant mechanism for the mixing of atmosphere and sea constituents. As such, the breaking process is crucial for the transfer of heat and momentum between air and sea. Air entrainment is an element of wave breaking responsible for the transmission of gases, particularly O_2 and CO_2, across the ocean's free-surface; a process aided by the local increase in turbulence and dissipation accompanying breaking. This process is not only vital to the survival of aquatic life and the preservation of good water quality, but it also serves a larger purpose in such phenomena as Earth's weather and climate. In fact, transfer of CO_2 from the atmosphere to the ocean is central to the global warming debate. Wave breaking also serves to transfer momentum and energy from wind to waves, and correspondingly from waves to sea. In breaking, water waves impart some of their momentum to currents and consequently aid in the generation and perpetuation

of ocean circulation. In addition, noise generated during the breaking process may also be harnessed for use as a diagnostic tool for air-sea interaction studies.

In the context of water wave studies, a deep-water wave is typically defined such that the ratio of the water depth to the wavelength is greater than 0.5 (Dean and Dalrymple, 1991). This implies that the water is sufficiently deep so as eliminate any direct effect of variations in bottom topography on the surface waves. In this sense, even small bodies of water, such as ponds and lakes, can support deep-water breaking waves. Breaking waves in deep water may be the result of instabilities created by the constructive interference of varying waves, interactions between waves and currents, and/or the influence of wind on the sea surface. In addition to the important issues surrounding general wave breaking, deep-water wave breaking poses added concerns to scientists, engineers, and laymen alike. Of utmost interest to commercial and recreational sea-goers is the safety of their vessels. Wave breaking on boats can lead to severe damage or even total loss, and even the most modern ships are susceptible to the intense forces associated with such breaking episodes. Similarly, deep-water wave breaking events can result in severe dynamical loadings on offshore structures and thus are of great concern to design engineers.

The dynamics regarding deep-water wave breaking have been studied in various capacities ranging from observational field studies, to laboratory investigations, and, more recently, to numerical modeling. Field studies have proven a difficult means by which to quantify deep-water wave breaking. The most significant visual indication of wave breaking is “white-capping,” the visual evidence of air entrainment into the overturning wave. Wave breaking can occur, however, on centimeter scales. Such breakers are typically void of white-caps, rendering it problematic to distinguish them among a sea of waves. In addition, while there is little argument that waves break in deep water, there is discrepancy among investigators as to what constitutes the onset of breaking. Thus, these studies can pose added challenges in the comparison of results

due to both human judgment and the unsteady, nonlinear complexities inherent in wave breaking events.

Laboratory studies have provided a more controlled environment in which to consider this phenomenon. Such studies have led to many advances in our understanding of wave breaking in deep water and presently serve as the means by which to verify numerical simulations of this complex process. Still, the best approach to adopt in the generation of deep-water breaking waves in the laboratory remains unsettled, and these studies often overlook or ignore components of the wave generation process, such as wind input and currents, which are undoubtedly present in more realistic ocean conditions. In addition, the extreme nonlinear nature of these breakers, including generation of vorticity at the free-surface, rapid production of turbulence, air entrainment, and spray generation, makes individual wave characteristics difficult to measure.

Similar difficulties prove to be a hindrance in numerical simulations. The bulk of these studies involve 2D models, many of which are only capable of effectively capturing the dynamics of breaking waves up to the point of overturning before becoming numerically unstable. Typically, these models also have their basis in potential flow, and thus approximate or ignore many of the nonlinear characteristics of wave breaking in deep water. Discussion as to the most efficient means by which to represent the free-surface and domain boundary conditions are ongoing. What 3D models do exist in the realm of wave breaking have experienced some success in the simulation of shallow-water wave breaking over a varying bed but have not yet, to our knowledge, been applied to simulate deep-water wave breaking.

We have modified a fully 3D, finite-difference, time-dependent model, entitled TRUCHAS, for use in this study. This model is capable of simulating not only the dynamics of the water column up to, during, and after wave breaking, but also the flow of air above the free-surface throughout the breaking process. Our simulations mirror a

laboratory experiment conducted by our partners Mark Donelan and Brian Haus at the Center for Air-Sea Interaction at the University of Miami, who created such deep-water breaking waves in their Air-Sea Interaction Salt-Water Tank (ASIST). Results from the laboratory experiment are compared with our model results to verify the numerical computations. While we do not pretend that this model is the only or most efficient way of capturing deep-water wave breaking events, we do hope that our findings may further the scientific and engineering communities in the quest to understand the intriguing and complex dynamics of wave breaking in the deep-water realm.

1.2 Literature Survey

Wave breaking in deep water has been a subject of interest for quite some time, and despite what remains to be clarified of this complex phenomenon, much has already been learned about wave dynamics in this regime. Banner and Peregrine (1993) provide a comprehensive overview of the deep-water wave breaking process, from a definition of deep-water waves to a physical description of the various types of breaking events. Not only does this work provide a summary of the many methods implemented in both the field and laboratory environments to study deep-water waves, but it also includes a discussion of the theoretical aspects employed in the quest to better describe the unsteady process. The work of Duncan (2001) is an in-depth examination of spilling breakers; the breaking type that our study is designed to investigate. Drawing from the experimental and theoretical studies of others, Duncan (2001) documents the evolution of a spilling breaker from initial deformation to the turbulence generated both during and post-breaking. While providing information for spilling breakers at all depths, this study pays particular attention to unsteady breakers, with a deep-water analysis relevant to our study. Works by Longuet-Higgins (1978), Yuen and Lake (1980), and Kjeldsen and Myrhaug (1980) examine the mechanisms whereby steep waves in deep water are generated, along with a thorough analysis of wave asymmetry, steepness, profile and particle velocities, and other nonlinear

effects inherent in deep-water breaking waves. Implications of deep-water wave breaking, including the significant role of this process in air-sea interaction and Earth's climate and circulation, are noted by Csanady (2001) and Melville (1996). A detailed look at the specific means that have been employed to study this phenomenon, both experimentally and numerically, will provide the reader with an understanding of the vision behind the multiple methods of investigation upon which our study relies.

Observational field studies of deep-water wave breaking, such as that carried out by Holthuijsen and Herbers (1986), are often limited solely to the examination of white-capping events; this phenomenon being the most reliable means by which to identify a breaking event. Such studies, however, are highly subjective, and illustrate the main motivation behind most physical studies being conducted in controlled laboratory settings. VanDorn and Pazan (1975) initiated the practice of investigating the breaking dynamics of deep-water surface waves in controlled, reproducible laboratory conditions. Single-frequency, periodic, deep-water waves trains were generated by a tape-controlled paddle and made to converge and break in a tapered channel. While much information regarding velocity and profile evolutions was ascertained, neglect of such parameters as randomness of waves, influence of wind shear, and the dynamics of wave trains of varying frequencies establish this study as introductory at best. Perhaps the most comprehensive deep-water wave breaking study to date is that of Rapp and Melville (1990), in which the authors used a focusing technique to ensure breaking. Wave-wave interaction induced breaking resulted from linearly decreasing the wavemaker frequency, thus increasing the group velocity of the generated waves and focusing wave energy longitudinally at a predetermined time and location. A multitude of breaking characteristics, including velocity, rate and extent of turbulent mixing, and net loss of total mass flux, horizontal momentum flux, and energy flux were considered. Rapp and Melville (1990) cite reflections due to the finite-length channel, disregard of the effects of wind, and errors occurring in the

scale-up of results to a more realistic domain as disadvantages of this technique. Still, their work remains a staple in the scientific and oceanographic community to which the results of modern studies are compared.

A similar method of wave generation was employed by Kway *et al.* (1998), who correlated many wave breaking characteristics to the spectral slope of the higher frequency components of the wave energy, offering this parameter as a more reliable determination of wave breaking than steepness alone. Non-negligible energy loss was attributed to dissipation at the channel walls and bottom during this study, and the determination of surface elevation within the breaking region was complicated by the entrainment of air. A further examination of the energy associated with the nonlinear evolution and subsequent breaking of deep-water wave groups is provided by Tulin and Waseda (1999), who attempted to correct for limitations in previous studies by generating wave trains with a range of steepnesses and by employing a wider wavetank to diminish wall effects. Still, multiple reflections between beach and wavemaker, as well as cross-tank disturbances, were seen to bias results if measurements were not taken within 3-4 round-trips of the wavemaker. Melville *et al.* (2002) also utilized the methods described by Rapp and Melville (1990) to investigate a positive mean vorticity throughout the volume of fluid that is mixed downward under the deep-water breaking waves, and found that this indicated a flow in the direction of wave propagation at the surface with a return flow near the bed. Consistently negative Reynolds stresses found during this study indicated positive horizontal momentum being transported downward through the water column during breaking, and a downstream propagating eddy generated during the breaking process is also of interest. Despite these intriguing observations, it is worthy to note that although the authors deem the importance trivial, these measurements were conducted under conditions in which the individual waves were of the deep-water variety, but wave groups were intermediate or even shallow in depth.

An early investigation of air-sea interaction during breaking of interest to our analysis was conducted by Zagustin (1972), who simulated the dynamics between two fluids during breaking using a mercury-water model. Waves were initiated at the interface, albeit rather crudely, in three sections by varying the movement of the bed in each section with the use of wheels of different diameters connected by chains. Zagustin (1972) observed a circulation flow pattern above each breaking water wave. The author attributed the transfer of energy from air flow to the water wave to this circulation pattern. Though only examined briefly in the context of this work, our model does verify the existence of this flow pattern in the air surrounding the breaking waves.

Such laboratory analyses paved the way for the exploration of the deep-water wave breaking process by numerical means. Two-dimensional models, still widely employed today, were first applied to the deep-water environment by such pioneers as Chu and Mei (1971), who used numerical simulations to observe the nonlinear evolution of deep-water wave trains. Longuet-Higgins and Cokelet (1976) were the first to report computations of the evolution up to breaking of fully nonlinear, unsteady deep-water waves. This study, however, neglects both surface tension and viscosity, and is only valid until the breaking wave reaches overturning, at which point the model becomes unstable. Similar problems are experienced in the computations given by Henderson *et al.* (1999) and Dommermuth *et al.* (1988), whereby effective analysis of breaking is hindered by model instabilities apparent as the wave initiates overturning. Longuet-Higgins and Cokelet (1976) also note that in each of their computations saw-toothed instabilities occur. While the wave profile can be rendered smooth via a smoothing mechanism, its origin is unknown, and the authors suggest the absence of viscosity within their model computations as a plausible explanation. Dommermuth *et al.* (1988) suggest the Lagrangian method of particle tracking employed by Longuet-Higgins and Cokelet (1976) concentrates points of the

free-surface in regions of high velocity gradients, where small errors in the computed velocity potential can lead to large errors in particle velocities, thus producing the saw-tooth appearance. This instability is avoided by Dommermuth *et al.* (1988) by employing a regridding mechanism. However, wave reflection from the endwall of the computational tank provides a new source of error in this numerical approach.

Both Banner and Tian (1998) and Song and Banner (2002) examine the onset of breaking for 2D nonlinear deep-water wave trains via a boundary element method. Banner and Tian (1998) gives steepness values higher than those typically reported of dominant ocean wave breakers, which may indicate that key parameters such as the influence of shear from the air and/or 3D effects not included in this 2D model are of great importance in the deep-water wave breaking process. Song and Banner (2002) employ the boundary element method to investigate controlled breaking via a "chirped" wave packet similar to the those generated by Rapp and Melville (1990) in the laboratory; a scenario very similar to that which we examine in our present study. Again, computations in this technique are limited to the realm up to and including overturning and are thus incapable of effectively representing the entire breaking process, during which many of the most important elements are generated or intensified during the turbulent post-breaking phase. As a solution to the substantial shortcomings of the boundary element method in explaining the complex breaking process, Miyata (1986) suggests the finite-difference method as the superior technique in modeling wave breaking scenarios. The robustness of this method was verified by Chen *et al.* (1999), who employed a piecewise linear version of the volume of fluid method (Liu and Lin, 1997) using finite-differences to simulate the breaking process of deep-water plungers including overturning and splash-up. Though a much more comprehensive study than its predecessors, this analysis lacks a turbulence model, and consequently is apt to miss key components of the post-breaking process. In addition, the 2D nature of the model itself is a hindrance. It is well documented that 2D turbulence is less

dissipative than that of three dimensions and that small scale structures generated during the breaking process differ greatly in two and three dimensions, and thus are likely to effect the vorticity field and energy dissipation in different manners.

Recent attempts to improve upon these 2D models have brought new information to light regarding the complex nature of breaking deep-water waves. Song and Sirviente (2004) assessed the role of surface tension in deep-water wave breaking, a parameter that until this point had not been considered in most numerical models. Model results show that including surface tension in numerical computations brings about a significant reduction in jet intensity and air entrainment, and thus contributes significantly to the breaking process. It should be noted, however, that parameters used in this two-fluid study are not always representative of ocean waves, but results are expected to correlate well with realistic breaking events. Improvements in the calculation of velocity fields beneath unsteady waves are given by Donelan *et al.* (1992). These authors address the issue that previously employed techniques, dependent upon the relation between sea surface elevation and velocity potential as given by linear theory, assume a free-surface boundary condition that is applied at the mean water level and not at the actual free surface. Donelan *et al.* (1992) instead offer a solution based on the linear superposition of a sum of freely propagating wavetrains. In this approach, the free-surface at a particular location is given as the linear combination of all of the wave components present at that instant, and thus has a velocity at the free-surface that is reflective of this superposition. This method is utilized in calculating the free-surface elevation and particle velocities input into our model. Lin and Liu (1999) offer alternate methods by which to generate any number of specific wave trains via an internal mass source function. This internal "wavemaker" does not interfere with reflected waves and thus is suitable for use in long duration simulations. Advances to include the third dimension in numerical approaches to studying water wave breaking have most recently been made by Grilli

et al. (2001), Xue *et al.* (2001), and Viausser *et al.* (2003), each not without limitation. Grilli *et al.* (2001) describe shoaling waves over complex bottom topography using a boundary element method. Accordingly, the numerical computations are subject to the same constraints of their 2D counterparts and can only be carried out to the point of overturning. Xue *et al.* (2001), also opting to adopt the boundary element method, experienced the same restraints, finding that accurate simulation of breaking is unattainable as breakers reach late stages of overturning. By coupling the boundary element method with a volume of fluid approach for the post-overturning stages of breaking, Viausser *et al.* (2003) were able to give results for breaking waves throughout the entire range of the breaking process. Viausser *et al.* (2003) used this technique to explore the dynamics of shoaling waves on sloping beaches, and therefore give no insight as to the 3D details of breaking waves in deep water. The effects of surface tension, air dynamics, and viscosity are also neglected in this study, leaving need for a more robust 3D numerical model to be developed.

1.3 Organization

In the subsequent chapters, we provide information regarding a new 3D model and its ability to accurately resolve physical characteristics and nonlinear dynamics associated with spilling waves in deep water. Chapter 2 is comprised of model parameters, capacities, and limitations. The governing equations and user-specified controls used in this study are presented within this chapter. Also included in Chapter 2 are the specifics of our improved boundary condition for wave forcing as well as the outflow conditions adopted for this study. A brief description of the laboratory investigation conducted by Donelan and Haus, information regarding the adaptation of our model to simulate this experiment, and the physical and numerical specifications of our simulations can all be found in Chapter 3. Both laboratory results and the outcome of our numerical efforts will be examined in Chapter 4. This chapter also includes a brief aside into the flow patterns in the air surrounding the water waves.

An analysis of our numerical computations and a discussion of the implications of our findings, in conjunction with concluding remarks on the capability of the numerical model to accurately depict wave breaking in deep water can be found in Chapter 5. Also contained within this chapter is a summary of numerical studies experiencing outcomes similar to those obtained in this investigation and the implications of their findings. A promising capability of our model, not examined within the scope of this study, is its capacity to simulate the flow of wind over the water surface, thus creating wind-generated waves. This finding is briefly explored in the Appendix on page 78, but the full potential of this discovery is ultimately left to a future study.

CHAPTER 2
METHODOLOGY

2.1 Model Dynamics

Capable of producing detailed simulations of flow regimes involving numerous fluids of varying density, TRUCHAS is a 3D, finite difference, time-dependent numerical model of great competence. A successor of such computational fluid dynamics (CFD) models as the SOLA-VOF Method and RIPPLE, TRUCHAS is the result of 40 years of advancement dating back to the debut of the Marker-and-Cell (MAC) Method for incompressible multiphase flows in 1965 (Team, 2004) . In similar fashion to the SOLA-VOF methodology, TRUCHAS couples its algorithms with a volume tracking method to accurately evaluate the fraction of each fluid material within every mesh cell. TRUCHAS also employs the Continuum Surface Force (CSF) Method, a surface tension model utilized by RIPPLE in which the effects of surface tension are applied to fluid elements located within the numerically resolvable transition regions. This localized volume force is readily included into the algorithm by applying an extra body force into the momentum equation (Kothe *et al.*, 1991). Advances in projection methods and increased efficiency in solving linear systems of equations, coupled with the methodology mentioned above, have resulted in TRUCHAS, the robust numerical model considered in this work. Numerous algorithms included within the the model's vast code allow for the solution and modeling of such phenomena as heat transfer and phase changes, chemical reactions, solid mechanics, electromagnetics, and fluid dynamics. We wish to focus on the fluid dynamics algorithm of the model.

2.2 Assumptions and Approximations

The fluid dynamics algorithm included within TRUCHAS operates on the basic assumption that the fluids are incompressible unless designated as void space, defined as an idealized material having zero density and therefore infinite compressibility. TRUCHAS also employs the Continuum Hypothesis, as molecular activity is averaged over small spatial and temporal scales. Moreover, TRUCHAS assumes that the flow of all fluids included within the simulation can be captured and evaluated on a single velocity field at any given point within the flow regime. Thus, boundary layers, often of a much smaller scale than the overall flow dimensions, are resolved by the computational mesh.

In addition to the aforementioned assumptions, TRUCHAS also exploits many approximations to simplify its governing flow equations. Those most pertinent to this work include the assumption that all fluids can be considered Newtonian. Thus, viscous shear stress is assumed to be a linear function of the shear rate. TRUCHAS also approximates turbulent flow regimes by calculating this viscous stress from the averaged molecular viscosity in each cell, a fluid property designated by the user, and then coupling this stress with a simple algebraic turbulence closure model. The advection of momentum by TRUCHAS is achieved through the use of a first order scheme that utilizes old time level velocity values, but densities consistent with updated material volume fractions. TRUCHAS operates under a semi-implicit time scheme to produce a stable solution that is 1st order accurate in time. This is accomplished by treating the pressure gradient implicitly, while allowing all other forces to be treated explicitly (Team, 2004). Spatial discretization within the mesh is conducted via a combination of both 1st and 2nd order accurate derivations. Advection terms, however, remain 1st order accurate, as is necessary for computations involving interfaces between different fluids. In addition, flow specifics rely heavily on the precision of input

variables, such as fluid densities, as defined by the user, in CGS notation. A more comprehensive evaluation of the flow analysis and its details follows.

2.3 Governing Equations

TRUCHAS seeks to solve the Incompressible Navier-Stokes Equations in its determination of fluid flow. Said equations can be represented as in a single Conservation of Momentum equation, shown in Eq. 2–1.

$$\frac{\partial(\rho\vec{u})}{\partial t} + \nabla \cdot (\rho\vec{u}\vec{u}) = -\nabla p + \nabla \cdot \tilde{\tau} + f_B + f_S + f_D \tag{2–1}$$

where
$\vec{u}$ = fluid velocity
ρ = density
p = pressure
$\tilde{\tau}$ = shear stress tensor
f_B = body forces, i.e. gravity
f_S = any surface forces
f_D = drag force included to describe flow in the vicinity of a solid or open boundary

Operating under the assumptions mentioned in the previous section, TRUCHAS can further define the shear stress rate as a function of the dynamic viscosity of the fluid, a variable set by the user at the onset of the simulation, as depicted in Eq. 2–2.

$$\tilde{\tau} = \mu(\nabla\vec{u} + \nabla^T\vec{u}) \tag{2–2}$$

where
μ = dynamic viscosity
T = operation of transpose

Similarly, TRUCHAS can further simplify the surface forces term, f_S, of Eq. 2–1 by recognizing that the only surface force employed in the fluid flow simulations is surface tension. TRUCHAS defines this constituent as a volumetric force at work on fluid elements in the vicinity of a surface, S, as illustrated in Eq. 2–3.

$$f_S = \sigma\kappa\bar{n_S}\delta_S \tag{2–3}$$

where

$\sigma =$ surface tension coefficient, as specified by the user
$\kappa =$ total curvature of an interface
$\bar{n_S} =$ a unit normal to S
$\delta_S =$ Dirac delta function

Conservation of mass is then maintained via Eq. 2–4.

$$\frac{\partial \rho}{\partial t} + \nabla \cdot (\rho \vec{u}) = 0 \tag{2–4}$$

Despite the previously-stated assertion that all fluids considered by TRUCHAS are assumed incompressible, the flow algorithm inherent within TRUCHAS is capable of handling multiple immiscible fluids, all of varying density, within a single domain. As such, TRUCHAS chooses to preserve the ρ term within the bracketed terms on the left-hand-side of Eq. 2–1 (Team, 2004). Within a single fluid material, however, ρ is expected to remain constant throughout time, as represented by Eq. 2–5.

$$\frac{D\rho}{Dt} = 0 \tag{2–5}$$

Utilizing this constraint, Eq. 2–4 can be rewritten as the Continuity Equation, Eq. 2–6.

$$\nabla \cdot \vec{u} = 0 \tag{2–6}$$

In its final expression, Eq. 2–1 is simply a Eulerian form of conservation of momentum, conditional on the incompressibility requirement imposed by Eq. 2–6. Furthermore, Eq. 2–4, in its simplest explanation, details the transport of various fluids throughout the system (Team, 2004).

2.4 Flow Algorithm

The flow algorithm inherent in TRUCHAS relies heavily on a volume tracking method to quantify and to advect material properties throughout the numerical domain. More than simply generating new values of fractional volume for each fluid, this step also allows TRUCHAS to note the volumes of fluids moving across cell faces from one time step to the next. Said volumes then become the means by which all

other quantities are advected throughout the mesh. This acts to ensure that the varied transport equations employed by TRUCHAS remain consistent.

Though TRUCHAS is capable of handling various domain types, this work utilizes a simple rectangular mesh. A typical grid cell, including the coordinate system designated by TRUCHAS and the corresponding face centered velocities, is given in Fig. 2–1. Material volume fractions are evaluated in each of these numerical cells for

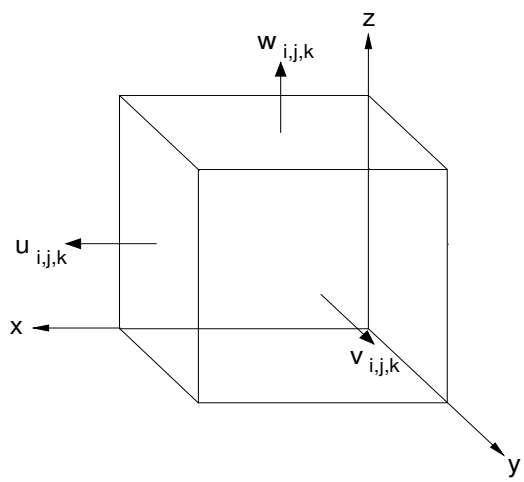

Figure 2–1: A computational cell depicting the coordinate system and face centered velocities computed by TRUCHAS.

each time step of the simulation, and volume fluxes across cells are also noted. Given the new volume fractions for each fluid, material properties including density and viscosity are then assessed within each cell. Such values can then be implemented in the evaluation of velocity and pressure fields throughout the domain. A more detailed analysis of this involved process is outlined in the following subsections.

2.4.1 Free-Surface Tracking

TRUCHAS initiates its flow algorithm with the multidimensional Piecewise Linear Interface Calculation (PLIC) method to determine the volume of each fluid in each mesh cell. Free-surface tracking is accomplished within TRUCHAS by representing the fluid interfaces with volume fractions, as explained by Team (2004). This method aims to resolve the Conservation of Mass equation, Eq. 2–4, for ρ^{n+1} using u_f^n. Initiation

of this process involves the defining of a volume fraction, f_k, as the fraction of a cell volume V occupied by fluid k, as depicted in Eq. 2–7.

$$f_k = V_k/V \tag{2–7}$$

Correlation of cell density to Eq. 2–7 yields Eq. 2–8.

$$\rho = \sum f_k \rho_k \tag{2–8}$$

This, in return, leads to a new definition of Eq. 2–4, Eq. 2–9.

$$\frac{\partial(f_k \rho_k)}{\partial t} + \nabla \cdot (f_k \rho_k \vec{u}) = 0 \tag{2–9}$$

Furthermore, utilizing the knowledge that ρ_k is constant, an evolution equation, Eq. 2–10, can be ascertained.

$$\frac{\partial f_k}{\partial t} + \nabla \cdot (f_k \vec{u}) = 0 \tag{2–10}$$

where
$\vec{u}$ = fluid velocity
f_k = volume fraction of fluid k

The solution of f_k represents the presence, or conversely the absence, of a particular fluid element within each mesh cell. Thus, Eq. 2–10 is essentially an evolution equation for the location of each fluid. The volume fractions of each fluid are bounded within the range $0 \leq f_k \leq 1$ as depicted below.

$$f_k = \begin{cases} 1 & \text{inside fluid k} \\ > 0, < 1 & \text{at the fluid k interface} \\ 0 & \text{outside fluid k} \end{cases}$$

As Eq. 2–10 is continually resolved within the algorithm, TRUCHAS tracks fluid volumes and marches them forward in time with each successive calculation.

2.4.2 Volume Tracking Algorithm

The PLIC Volume Tracking Algorithm, mentioned in the previous subsection, allows for the solution of Eq. 2–10 in terms of f_k^{n+1}. The complete resolution of this algorithm includes two separate steps. The initial step consists of a planar reconstruction of fluid-fluid interfaces within each mesh cell. Working under the reconstructed interface geometry assumption, interfaces between different fluids are constructed using the fluid volume data such that the geometry of the interface is piecewise linear, or planar. As detailed by Team (2004), this reconstruction involves an exact correlation to f_k^n as well as to approximations of the locations of the fluid interfaces based upon gradients of the f_k^n. The second phase of the tracking algorithm entails a computation of the volume fluxes of all fluids across cell faces. Via a simple multiplication by Δt, these volume fluxes can reveal the volume of each fluid material crossing every cell face. After a spatial smoothing of the f_k field has been implemented, this information is used to update the volume fractions of each fluid constituent throughout every cell in the mesh, and, should the need arise, this information may also be utilized to track the transport of chemicals, temperature, or other quantities the user may wish to model. For instance, such mesh cell attributes as fluid density and viscosity are calculated as averages of the various fluid components within that specific cell.

An advantageous quality central to TRUCHAS's flow algorithm is its allowance of sub-cycling. This process, by which the volume tracking algorithm is allowed to run multiple passes within a single time step, vastly improves the accuracy of the solution. A benefit to this added capacity is that TRUCHAS is able to track fluid elements through more than one mesh cell during each time step. This capability is of great value throughout the domain where the fluid interface may be propagating at an angle to cell faces.

2.4.3 Pressure and Velocity Field Evaluations

Having determined the fluid properties unique to each mesh cell, TRUCHAS embarks upon a 4-step evaluation of the new velocity and pressure fields. The first stage in this process involves the time discretization of the momentum equation, Eq. 2–1, in which predetermined values calculated as a combination of velocity, temperature, and species concentration values retained from the previous time step are used along with fluid volume fractions and material transfer volumes from the volume tracking step to approximate the new cell centered velocities via a forward Euler time step. The resulting time-discretized momentum equation can be divided into two parts, a predictor step and a projection step.

In the predictor step, an interim "predicted" velocity value is introduced and solved for, as shown in Eq. 2–11.

$$\frac{\rho^{n+1}u^* - \rho^n u^n}{\Delta t} = -\nabla\cdot(\rho u u)^n + \nabla\cdot(\mu^{n+1}(\nabla u + \nabla^T u)) + f_S^{n+1} + f_D^{n+1} - \nabla P^n + f_B^n \quad (2\text{–}11)$$

where
$u^* =$ an interim "predicted" velocity

Once a value for u^* has been established, a pressure correction, defined as $\delta P^{n+1} = P^{n+1} - P^n$ is evaluated via Eq. 2–12.

$$\nabla \cdot \frac{\nabla \delta P^{n+1}}{\rho^{n+1}} = \nabla \cdot (\frac{u^*}{\Delta t}) \quad (2\text{–}12)$$

The solution of Eq. 2–12 for δP^{n+1} provides the pressure correction needed to ensure that the divergence within each mesh cell remains zero, or that u^{n+1}satisfies continuity. This pressure change is then used to solve the projection equation, given in Eq. 2–13, for the cell-centered velocity at the new time.

$$\frac{\rho^{n+1}u^{n+1} - \rho^{n+1}u^*}{\Delta t} = -\nabla \delta P^{n+1} + f_B^{n+1} + f_B^n \quad (2\text{–}13)$$

Finally, $P^{n+1} = P^n + \delta P^{n+1}$ is used to estimate the pressure field for use in Eq. 2–11 for the next time step.

Incorporated into this process are the explicit approximations of body forces, as well as implicit approximations to viscous and drag forces which act to aid in the stability of the simulation. Drag forces are determined from the assumption that they are proportional to the velocity components previously estimated. Any viscous forces are found by averaging velocity values from the previous time step with velocity values from the intermediate time level *, in conjunction with the assigned fluid viscosity values initially designated by the user. The net viscous stress for each mesh cell is calculated as a sum of the dot product of the velocity gradient multiplied by the face area with the face normal vector, as given in Eq. 2–14.

$$\vec{F}_v = \sum_f \mu_f A_f [\hat{n}_f \cdot (\nabla \vec{u} + \nabla^T \vec{u})] \tag{2–14}$$

where
$\vec{F}_v$ = viscous stress
μ_f = viscosity at the face
A_f = face area
$\hat{n}_f$ = face normal vector

As the velocity gradient is first order accurate, calculated via a least squares method, the resulting viscous stress will have second order errors. Such approximations as those outlined above result in the necessity to solve a linear system of equations in most calculations (Team, 2004).

During the second phase of this evaluation, TRUCHAS determines cell face velocities from the cell centered velocities ascertained in the previous step. Once cell face velocities are established, body force accelerations are then applied to the system. The pressure field is updated in the third step, as TRUCHAS again solves for the pressure field correction needed to eradicate the velocity divergence in every mesh cell. Finally, TRUCHAS adjusts its previously determined cell centered velocity field by averaging the changes in pressure field, calculated in step 3, across each cell

face. Successful realization of the four aforementioned steps achieves new velocity and pressure fields that are fully updated using the forward Euler time scheme (Team, 2004).

2.4.4 Acceleration Technique

As Fletcher (1991) asserts, all iterative techniques can be simply stated as procedures for successively modifying an initial guess such that the solution is systematically approached. TRUCHAS has the capacity to employ many such preconditioning algorithms to aid in its solution of the pressure and velocity fields. The acceleration techniques available to the user include a Multistep Weighted Jacobi method, Symmetric Successive Over-Relaxation (SOR), Incomplete LU Factorization, LU Decomposition, Conjugate Gradients and a Multigrid Method. For our purposes, we found the Multigrid Method to be the most time efficient and accurate preconditioning method. Accordingly, all results presented in this work reflect this acceleration algorithm.

The Multigrid procedure is most easily exemplified by assuming a grid spacing of $\mathrm{h_k}$ upon which a finite difference approach is used to solve

$$L * U = F \tag{2–15}$$

where
$L, F =$ matrices

A new variable, u, is then introduced as an approximation to the above solution and is defined as

$$U = u + v \tag{2–16}$$

where
$v =$ the correction to u

At this point, Eq. 2–15 can be rewritten as

$$L * v = f \tag{2–17}$$

where

$$f = F - Lu \tag{2–18}$$

Eq. 2–17 is resolved on a grid with varying cell spacing. The final solution, U, can then be determined from Eq. 2–16 once v has converged to its final solution (Peyret and Taylor, 1985).

The procedure outlined above is described by Peyret and Taylor (1985) as a strategy involving the transformation of a fine grid solution to a coarse grid solution, and then back to the fine grid. Fletcher (1991) asserts that it is this particular progression that allows the Multigrid Method to be more efficient than many of its counterparts in iterating to convergence. Other relaxation procedures, including Jacobi, Gauss-Seidel and SOR, readily resolve high frequency error components in a few iterations. These methods, however, are ill-equipped to quickly remove the low frequency components of the error. Conversely, these low frequency errors common to a fine grid are transformed into high frequency components when shifted onto a coarse grid spacing. As such, the Multigrid Method acts to effectively utilize the high frequency smoothing intrinsic in the relaxation procedures.

2.4.5 Possible Source Errors

Plausible errors can be born from the finite resolution of any calculation. The initial generation of the flow geometry is one such instance in which statistical errors may present themselves. Such errors are the result of the Monte Carlo Method employed by TRUCHAS to evaluate the initial fraction of each fluid element present within every mesh cell. This algorithm generates a number of test points within every mesh cell in a random manner. It is then determined in which specific fluid's geometry the random point happens to lie, and the test point is labeled accordingly. The value of each mesh cell is then approximated via an assumption that the fractional volume of

the cell occupied by each specific fluid is equal to the fraction of generated test points within the cell bearing that specific fluid's label (Team, 2004).

In addition, errors may result from interface approximations. As the simulation is allowed to progress, the location and orientation of fluid-fluid and fluid-solid boundaries inside each mesh cell are evaluated solely from volume fractions. The inaccuracies produced in this process can be greatly reduced by increasing the resolution of the simulation. As may be expected, mesh cells containing more than two fluids require the generation of multiple interfaces. As such, these situations increase the potential for error within the flow geometry.

2.5 Creation of a Numerical Wavetank and Model Improvements

2.5.1 Wave Inflow Boundary Condition

An orthogonal wavetank with a numerical "wavemaker" was desired to accurately simulate the laboratory experiments conducted by Donelan and Haus at the University of Miami's ASIST. A new inflow boundary condition was added to TRUCHAS to allow for the time-dependent influx of waves into the domain, effectively acting as a wavemaker at the inflow (x = 0 cm) boundary of our computational mesh. Testing of this new boundary condition was accomplished on a 100 cm x 50 cm x 60 cm (x by y by z) mesh with cell numbers totaling 50 x 10 x 60. Equations detailing the motion of the free-surface, as well as the kinematics for water particles at any given depth, were specified everywhere within the first tenth of a cm in the x-direction. Taken from Dean and Dalrymple (1991), these linear equations (Eq. 2–19, Eq. 2–20, and Eq. 2–21) are given below, and represent free-surface displacement η, horizontal velocity u, and vertical velocity w, respectively. The cross-tank velocity, v, was taken as zero as there was assumed to be negligible movement across the numerical mesh.

$$\eta = \frac{H}{2} cos(kx - \sigma t) \tag{2–19}$$

$$u = \frac{H}{2}\sigma\frac{cosh(k(h+z))}{sinh(kh)}cos(kx - \sigma t) \tag{2–20}$$

$$w = \frac{H}{2}\sigma\frac{sinh(k(h+z))}{sinh(kh)}sin(kx - \sigma t) \tag{2–21}$$

where
$H =$ wave height
$k =$ wave number, defined as $2\pi/L$ where L is the wavelength
$\sigma =$ angular wave frequency, defined as $2\pi/T$ where T is the wave period
$t =$ time
$x =$ horizontal position
$z =$ vertical position, taken as zero at the free-surface with increasing negative values from the free-surface to the bed

Test runs were conducted with a wave height of 8 cm and 0.7 second period waves. The mean water level was set to 45 cm, yeilding a wave number of approximately $0.0823\mathrm{cm}^{-1}$. Such specifications ensured deep-water conditions for our simulations.

The horizontal and vertical velocities given above were applied at the inflow boundary only for those cells beneath the free-surface for each time step. A fluid density of $1\mathrm{g/cm}^3$, distinctive of water, was also specified within this region. Cells at the boundary above the free-surface were designated as air, with a density of $0.001\mathrm{g/cm}^3$ and zero horizontal and vertical inflow velocities. As such, any flow in the air above the free-surface is simply in response to the dynamics of the water column. The density of the cell on the boundary containing the free-surface was reflective of the vertical location of the free-surface within that cell. The density of water was multiplied by the fraction of the cell beneath the free-surface, while the remaining fraction of the cell was weighted by the density of air. The sum of these two fractions gave a good estimate of the density of the cell containing this interface.

Fig. 2–2 shows the initiation of a deep-water wave simulation utilizing these inflow equations. Numerical simulations model time-dependent wave trains which are uniform across the tank. These deep-water wave trains are directed to propagate along

the numerical tank, dissipate on a beach, and exit the computational domain through a constant-pressure outflow condition, further examined in the following section. Fig. 2–2 provides a visual depiction of the inflow of a deep-water uniform wave train

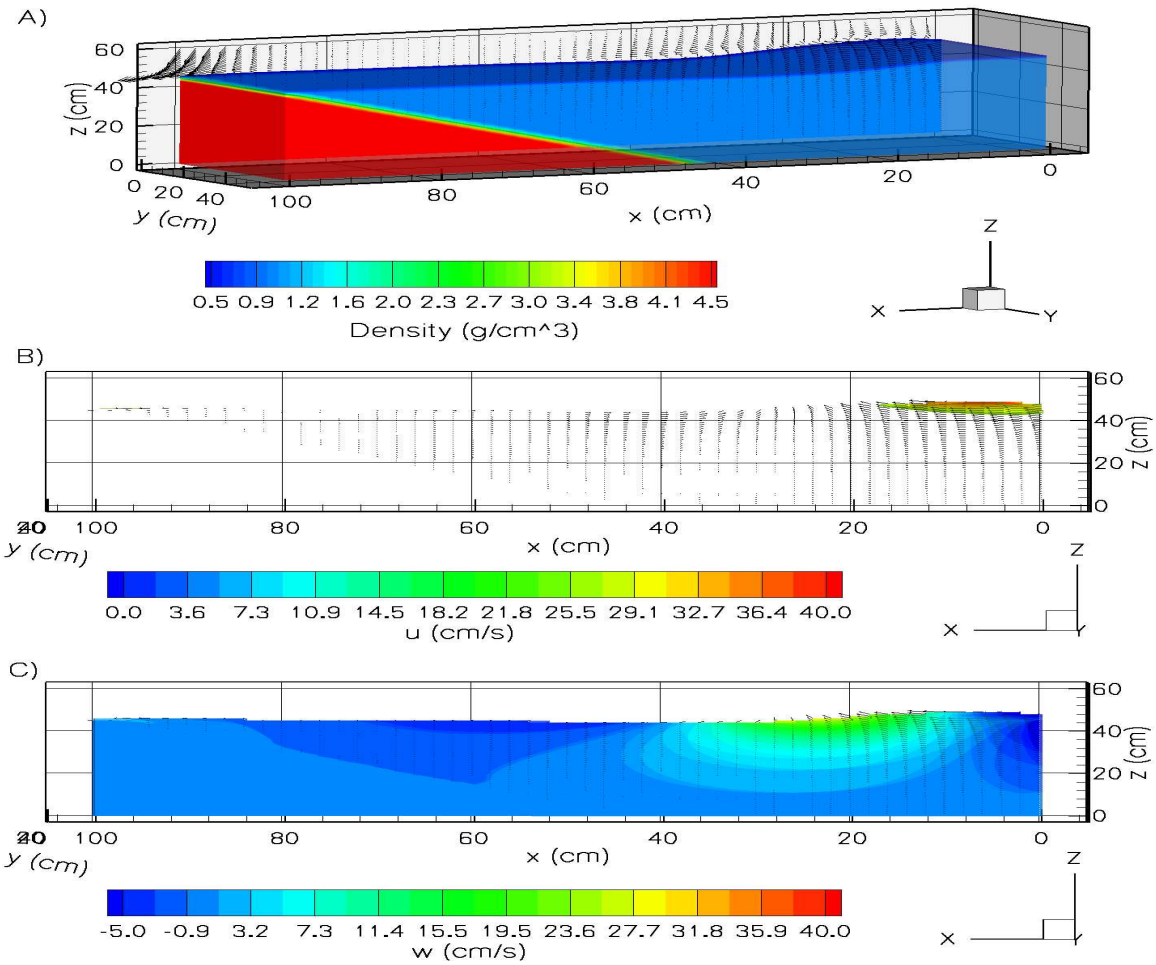

Figure 2–2: The initialization of a deep-water propagating wave train utilizing improved inflow boundary conditions. A visual of the numerical tank and inflow wave is shown in A), while velocity contours of B) u and C) w are displayed in a profile view and illustrate the depth-dependency of the velocity equations.

with a wave height of 8 cm as well as the horizontal and vertical velocity contours associated with these incoming waves. The linear nature of the wave equations requires that the velocity profiles decay with depth, a property that is clearly displayed in the figure. Thus, this improved forcing mechanism allows for the successful generation

of deep-water wave trains as given by linear theory, effectively acting as a numerical wavemaker with the added benefit of depth-dependency.

2.5.2 Outflow Conditions

In order to both conserve mass within the system as well as to maintain the mean water level at a constant depth, an outflow mechanism, by which excess mass may exit the domain, has been incorporated into the numerical scheme. First, a beach was created so as to dissipate wave energy and to minimize wave reflection at the far end of the numerical wavetank. The beach used in these initial stages is given a slope of 35 degrees. [1] The beach is designed to terminate on the outflow wall (x = 100 cm) at the mean water level. It is worthy to note that the PLIC Algorithm, detailed in Subsection 2.4.2, allows for a smooth beach face, rather than the staircase appearance often seen in other numerical models.

A constant-pressure boundary condition was then imposed on the end wall everywhere above the beach. This effectively created an outflow condition, as fluid can leave the domain through this ambient pressure zone. Fig. 2–3 shows a deep-water wave dissipating energy on the beach and then flowing out of the domain through the constant-pressure boundary. It is important to note that this is not a periodic boundary condition. Thus, waves flowing out of the tank at the outflow boundary do not reappear at the inflow boundary. Instead, this condition is a means by which to allow forcing of wave groups into the domain at the inflow boundary, while still satisfying conservation of mass and maintaining a mean water level.

The pressure throughout the domain is shown in Fig. 2–4. As apparent in this figure, a zero gage pressure boundary condition has also been specified at the lid of the

[1] Beach slopes were chosen with the simple constraint of sloping as gently as possible without extending more than approximately halfway along the base of the tank toward the inflow boundary.

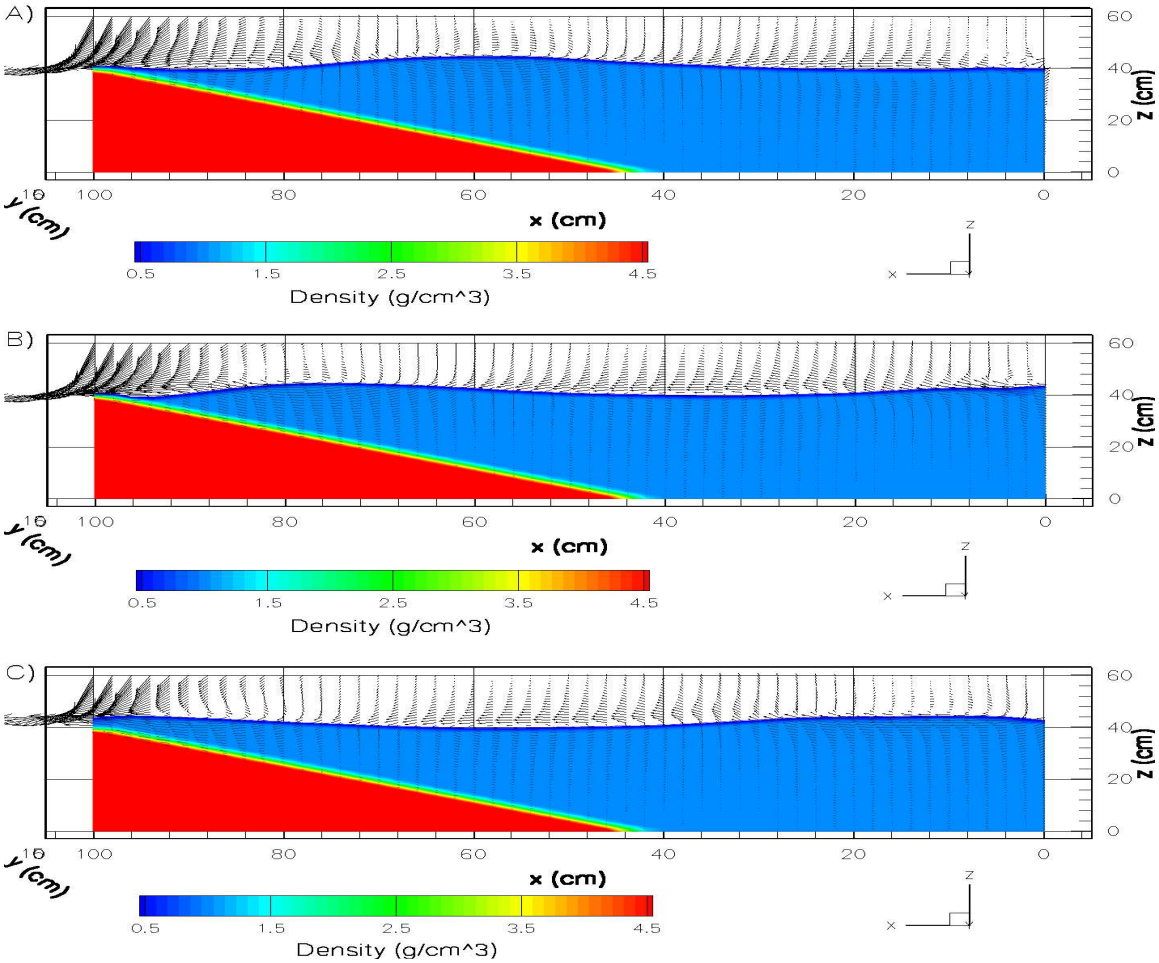

Figure 2–3: A profile view of outflow conditions for deep-water waves in the numerical tank, including a beach and the constant-pressure outflow zone. Time shots A), B), and C) are taken at consecutive 1/16 second intervals.

domain. This condition was applied in lieu of the typical rigid, free-slip boundary often used to characterize the lid of a numerical tank. We found the rigid lid too constricting to the flow of air above the water surface, as, regardless of the height of the tank, undesirable flow patterns above the water surface resulting from the flow of air into the domain through the constant-pressure outflow boundary were experienced. An ambient pressure, or open lid, condition significantly minimizes these unfavorable nonphysical patterns.

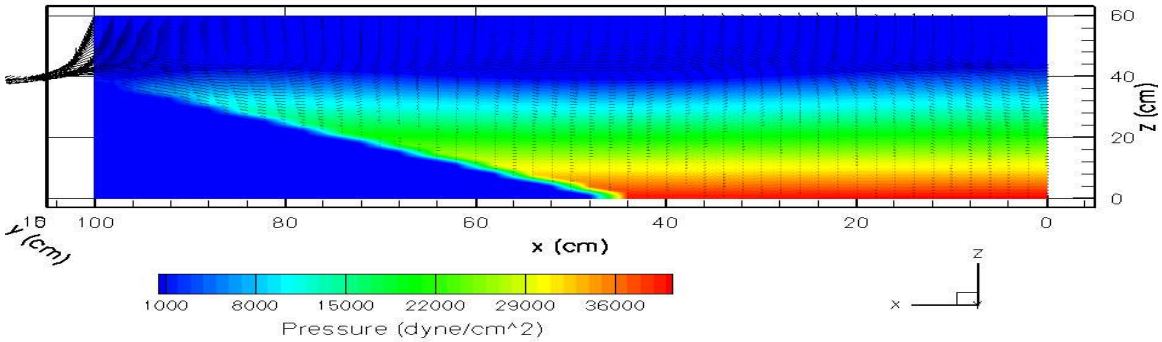

Figure 2–4: A plot of the pressure within the numerical wavetank. Note the zones of zero-pressure above the beach on the endwall and at the lid of the domain.

2.5.3 Boundary Conditions

Within the fluid flow dynamics inherit in TRUCHAS, fields to which boundary conditions may be applied are restricted to fluid velocity and pressure. TRUCHAS is currently unable to resolve such boundary conditions as Neumann, periodic, symmetric and hydrostatic, supplements to be added to future model versions. The numerical model is, however, capable of handling both no-slip and free-slip boundary conditions at mesh boundaries and on solid surfaces. In addition, Dirichlet boundary conditions may be applied at mesh boundaries for either pressure or velocity.

In conjunction with the special conditions mentioned previously, it was necessary only to utilize the no-slip and free-slip boundary conditions of TRUCHAS to complete our numerical wavetank. A no-slip boundary condition was enforced at the bottom of the tank as well as along the floor of the beach. As such, no horizontal velocity was permitted along the bed. Vertical velocity components were also required to be zero at these locations, as materials are forbidden to flow through the bottom of the tank or into the numerical beach. Free-slip boundary conditions were specified at the wavetank walls, allowing flow to move freely along these tank boundaries and thus keeping the flow as uniform as possible in the cross-tank direction and reducing dissipation and damping effects from the sidewalls.

CHAPTER 3
EXPERIMENTAL INVESTIGATIONS

To evaluate the competence of TRUCHAS to simulate deep-water breaking waves, a reliable data set is needed to which simulations can be compared. Mark Donelan and Brian Haus provided such data with a laboratory investigation conducted at the University of Miami's Center for Air-Sea Interaction. Donelan and Haus utilized Miami's Air-Sea Interaction Salt-Water Tank (ASIST) to conduct a controlled and detailed analysis of spilling breakers in deep water. Their comprehensive data set provided an attractive means by which to determine the capacity of our model to accurately predict and simulate wave heights, spilling characteristics, and turbulent generation associated with spilling breakers in a deep-water environment.[1]

3.1 ASIST Experiment

Miami's ASIST is a 15m by 1m by 1m stainless steel and acrylic tank with a programmable wavemaker. Photos of the laboratory setup, including some of the instruments used during the study are depicted in Fig. 3–1. Using the techniques of Rapp and Melville (1990), the wavemaker was programmed to produce a Gaussian wave packet in which waves were designed to coalesce and break at a specific point in the wavetank.

Detailed laboratory data can be collected within ASIST through a number of non-intrusive means. Most pertinent to this investigation, both in the model

[1] It should be noted that laboratory experiments, and consequently numerical simulations, were conducted with parameters characteristic of a transitional wave climate. In accordance with Melville *et al.* (2002), it is expected that results will lend themselves well to deep-water environments.

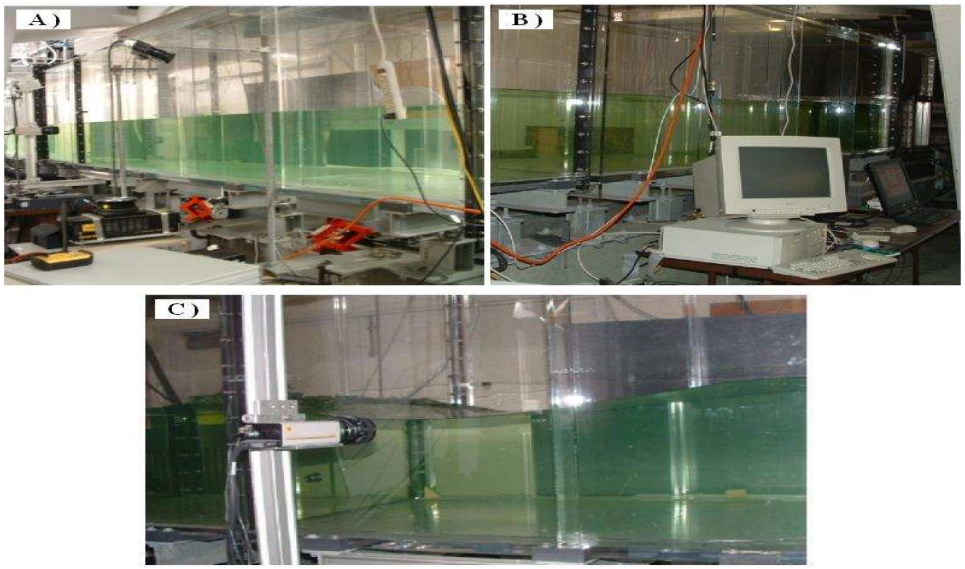

Figure 3–1: Pictures of Miami's ASIST setup for the laboratory investigation of deep-water spilling breakers. Views of the tank, including the PIV cameras and the computer station are given, respectively in A) and B), while camera positioning to monitor the free-surface displacement is depicted in C).

forcing and in the results comparison realms of this study, is the accurate collection of free-surface elevation data throughout the experiment. Measurements of the free-surface displacement were taken at two locations within the tank; location A, approximately 5.5 m from the wavemaker, and location B, at 8.5 m fetch, between which locations a spilling breaker was observed. Acquisition of the free-surface elevation at these given locations was accomplished with the use of multiple laser elevation gauges as well as a surface-focused camera, as depicted in Fig. 3–1. While the camera kept a visual record of surface elevation, the lasers acted to give a more detailed depiction of the interface characteristics. In a darkened setting, lasers were directed straight down onto the free-surface from a setting at the top of the wavetank. These beams of energy would then partially reflect off of the surface of the water column. Based on the orientation of the free-surface at any given instant, the reflected return signal would have a varying deflection angle. This "dancing" of the laser beams

could then be used to determine the components of the slope of the water surface at any given instant during the simulation.

Once the characteristics of the free-surface had been established, the details of the flow beneath the air-water interface could then be determined. Utilizing the methods outlined by Donelan *et al.* (1992), orbital velocities at centimeter increments below the free-surface were then tabulated from the elevation data at locations A and B. Readings were taken every 10 milliseconds, and a data file containing the time-series of free-surface elevation as well as u and w velocities at centimeter increments down the water column was created for each of the two locations. The data file for location A served as the means by which to force our model simulations, as documented in the following sections.

3.2 Model Adaptation

3.2.1 Numerical Setup

To accurately represent the experimental wavetank, a new numerical tank, depicted below in Fig. 3–2, was generated. The computational domain was 60 cm in height and 1 m cross-tank. Numerical simulations of the full 15 m laboratory tank were unnecessary to capture the important breaking aspects that we wished to study and would put unreasonable requirements on the computational time needed to run such simulations. Consequently, the numerical tank used in these simulations is just 4 m in length, providing an ample distance over which forcing and breaking events can occur. The mesh consisted of 106 cells along the tank in the x-direction, clustered with a 1 cm resolution within the breaking region and coarser (4-6 cm) resolution toward the boundaries. Cross-tank (in the y-direction), we made use of 24 total cells, also adopting a clustering method with very coarse 10 cm resolution at the tank walls fining to 2 cm resolution at the center of the domain. Uniform grid spacing was utilized in the z direction with 1 cm spacing increments. Such grid structuring allowed for a detailed view of the area of concern, while still keeping computational time within

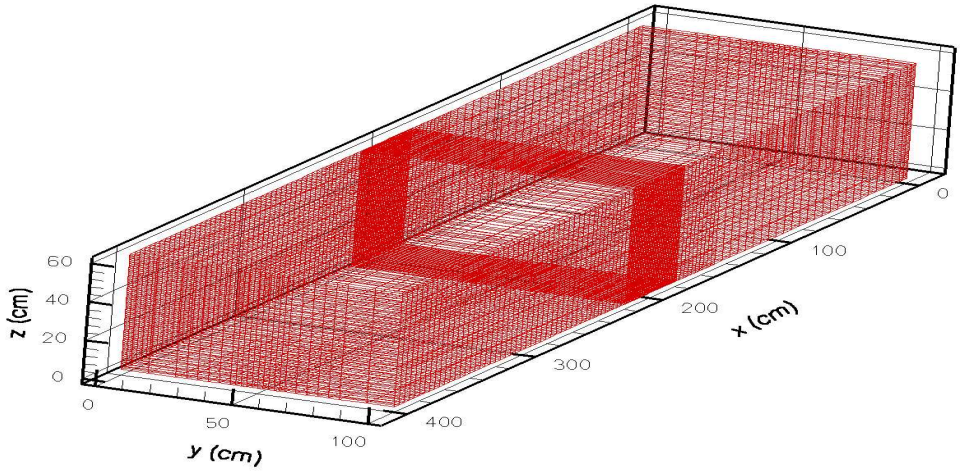

Figure 3–2: Numerical mesh used in TRUCHAS model simulations.

the reasonable realm of an approximate one week period. A summary of the various meshes tested and their computational cost is given in Subsection 3.3.2.

As detailed in the earlier simulations, the numerical tank was left open by adopting the ambient-pressure boundary condition at the top of the domain, keeping erratic flow patterns from developing in the air above the free-surface. A beach of slope 20 degrees, extending just shy of 1 m along the bed and terminating at the outflow boundary at the mean water level (36 cm) was included to dissipate waves and to encourage the flow of waves out of the system. A hybrid boundary condition was adopted at the outflow boundary: At 14 cm height above the beach, extending from the mean water level to 50 cm height, a constant-pressure region was enforced, allowing the flow of excess mass out of the tank. Along the same boundary wall ranging from 50 cm to the 60 cm tank height, a mandatory outflow of 0.5 cm/s was imposed. This condition was included to minimize the adverse propagation of air from the outflow boundary into the tank and against the outward traveling waves. No-slip conditions were included at the floor of the tank and along the bed of the beach. In contrast to the deep-water test cases mentioned in the previous chapter, however, no-slip conditions

were also enforced along the sidewalls of the tank in order to discourage the uniform behavior of waves across the tank and to promote 3D effects, thereby more accurately depicting the laboratory experiment.

3.2.2 Wave Forcing Using Laboratory Data

A Gaussian wave packet was forced at the inflow boundary as specified by the laboratory data measured at point A of ASIST provided by Donelan and Haus, and velocities output by TRUCHAS at the third gridpoint (x = 4 cm) were examined. It was desired that wave velocities output by the model at this along-tank location be consistent with the estimated laboratory wave velocities. The wave forcing computations added to TRUCHAS were introduced to the code within the projection module. As the projection module is invoked, TRUCHAS is allowed to adjust velocity values accordingly when velocity values entering a cell are greater than those leaving the cell. Hence, the laboratory velocities being introduced into the calculations via the projection module may experience some smoothing before final velocities are output at the third gridpoint, thereby giving way to slightly lower actual velocities versus forced velocities. As such, it became necessary to increase the forcing amplitude and corresponding velocities for the model so that the velocities output by TRUCHAS at the third grid point would accurately capture the expected laboratory velocities. After a number of trials, it was determined that model inflow velocities most closely resembled laboratory data at this location if TRUCHAS simulations were forced with the velocities, derived via Donelan *et al.* (1992)'s methods, associated with free-surface elevations scaled up by a factor of 1.1. Fig. 3–3 depicts the close relationship between measured laboratory velocities and TRUCHAS velocity values for both horizontal and vertical orbital velocities. It should be noted that velocity values shown in this figure were taken at a cross-tank location of y = 50 cm and at a vertical height of 29 cm for both laboratory and model data. The specified vertical height was chosen as it was the

first vertical grid cell beneath the mean water level that remained consistently within the water regime throughout time. As such, time series profiles remained continuous.

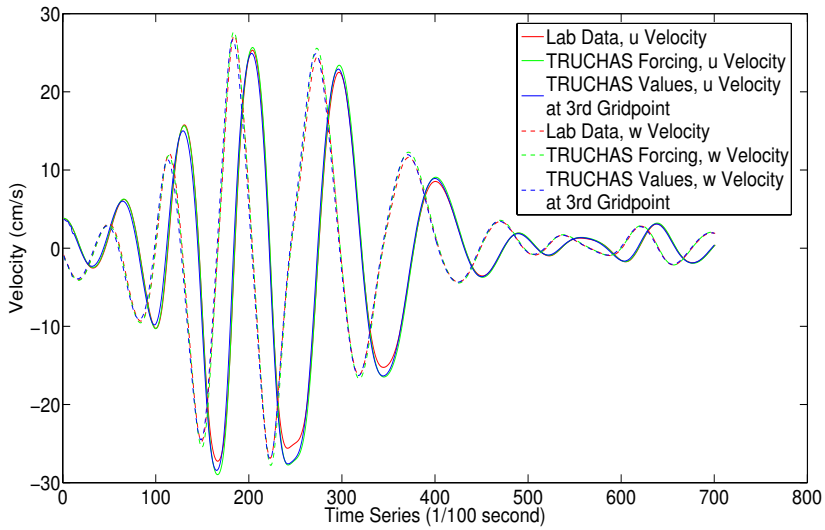

Figure 3–3: A representation of the numerical forcing and its comparison to laboratory values for both u and w velocity. The expected breaking wave is represented by the central wave form of the *u* velocity plot.

As seen in the figure, model velocities very closely resemble the laboratory data and only deviate slightly from calculated values of the *u* velocity at the trough of the waves. Such small differences could be attributed to slightly erroneous estimations in the methods utilized by laboratory investigators (Donelan *et al.*, 1992) to calculate the orbital velocities beneath the waves. For instance, as laboratory waves reach point A they have already developed nonlinearities, oftentimes which result in more peaked crests and shallower troughs. Such nonlinearities may be compunded as we increase the amplitude of the waves and then run the orbital velocity calculation program, thereby explaining the small discrepancy in horizontal trough velocities between the original and increased amplitude time series. We are confident that the model is forcing with the requested values, as the forcing velocities (represented by the green line in Fig. 3–3) very nearly replicate the velocity values computed by TRUCHAS at the third gridpoint (depicted as the blue line in Fig. 3–3). The almost imperceptible differences

between the forcing velocities and the velocities calculated at the first gridpoint are most likely due to numerical smoothing within the model computations.

3.3 Numerical Simulations

3.3.1 Specifying User Inputs

As alluded to in the previous chapter, TRUCHAS has available to its user many options to further dictate flow dynamics. Such user-specified options include the use of surface tension and algebraic turbulence models and more detailed information such as material densities and dynamic viscosities. These options are presented in Table 3–1, along with the specified inputs chosen for the final numerical simulations presented below. Test cases were conducted in which the ASIST experiment was simulated both

Table 3–1: A summary of model options available to the user and those specified for final simulations.

User Input	User Options	Final Simulations
Surface Tension Model	On, Off	Off
Algebraic Turbulence Model	On, Off	Off
Dynamic Viscosity	Default*, User Specified	0.0112g/(cm*s) (water), 1.79x10^{-4}g/(cm*s) (air)
Density	User Specified	$1.0\mathrm{g/cm^3}$ (water), $0.001\mathrm{g/cm^3}$ (air)

*Default value of dynamic viscosity for all materials = 0.0 g/(cm*s)

with and without activation of the surface tension model. Results indicated that an active surface tension model hindered simulation speed by a factor of approximately 1.5, yet there was no apparent benefit to using this model in the development and evolution of the deep-water wave packets. It is possible that surface tension effects are negligible for the principle dynamics at this scale of wave lengths and amplitudes. Thus, the surface tension model was turned off for the final numerical simulations. Similarly, runs were conducted to test the validity of the algebraic turbulence model. Although run times for the test case without the algebraic turbulence model were approximately 1.2 times faster than that with the turbulence model invoked, there did not appear to be any detriment to excluding the algebraic turbulence model from

our simulations. Given these results, final simulations were run without the algebraic turbulence model.[2] Test results also verified more reliable and accurate model results when material properties such as density and dynamic viscosity were appropriately specified for each material. Values of dynamic viscosity and density used in final simulations were taken from Munson *et al.* (2002). It should be noted that the beach, as defined by the user in these simulations, was given a density of $5.0\mathrm{g/cm}^3$ and was defined as an immobile solid, thereby having zero viscosity.

3.3.2 Computational Cost

As indicated previously, we found that the most efficient computational mesh to use in conducting our numerical experiments was a clustered mesh, fining to 1 cm by 2 cm by 1 cm resolution in the breaking region. As can be expected, finer resolution afforded us the ability to more accurately detail the smaller-scale flow dynamics. Coarser resolution at the mesh walls, however, significantly reduced the time it took to complete these runs. Presented in Table 3–2 are a number of test cases that were conducted and the computational expense of each 5 second simulation. As

Table 3–2: Five-second test simulations conducted to investigate the computational cost of improved mesh resolution.

Cell Aspect Ratio ($\delta x : \delta y : \delta z$)	Number of Cells (nx, ny, nz)	Tank Dimensions (x, y, z) (cm)	Computational Time (hrs)
2:1:1	50, 10, 10	100, 10, 10	4.17
2:1:0.5	100, 10, 20	200, 10, 10	25
2:1:1	200, 10, 60	400, 10, 60	125
2:2:1	200, 20, 60	400, 40, 60	166.67
2:1:1	150, 10, 100	300, 10, 100	457.5

is detailed in Table 3–2, the computational cost associated with meshes involving both an increased number of grid cells as well as finer resolution is a drastic increase in

[2] The decision to omit the algebraic turbulence model is further discussed in the following chapter.

the time needed to complete each simulation. As such, the clustered mesh detailed previously was adopted. Employing this computational domain, model simulations of 7 seconds are completed in approximately 7 days on the SGI-Origin 3400 computer running on a single processor.

3.3.3 Three-Dimensional Effects

It was hoped that by including no-slip boundary conditions at the sidewalls of the numerical wavetank, 3D effects would become apparent in the cross-tank dimension. To test this hypothesis, time averages of the mean velocity and total root mean square (rms) deviation from the mean velocity were performed. Following the examples illustrated by Lyons (1991), the y-averaged u, v, and w velocities were calculated by summing each velocity at each point across the tank with previous values and dividing by the number of y cells being summed over. A mean value for density was also obtained in this manner. The variance for each velocity was then tabulated by squaring the difference between an instantaneous velocity and the mean for each direction and dividing again by the total number of y cells being summed over. It should be noted that boundary nodes were excluded from these calculations to eliminate the effects of the no-slip sidewall conditions on the cross-tank velocity variance. Finally, an rms deviation from each mean, or standard deviation, was established by taking the square root of the variance. This value was multiplied by the mean density to eliminate large deviations in the air and to focus principally on variations within the water column. In addition, the root mean square deviations for each velocity were then summed to obtain a total rms value in the hopes that this value would be large enough to be of consequence in numerical simulations. A cross-tank view of the total rms deviation from the mean velocity is shown in Fig. 3–4 as the steepest point of the focused wave packet crosses the view plane. The skewed nature of the rms velocity field does indicate that there are some 3D effects in play as the focused wave crosses the plane of view. The significantly small values for rms velocity, however, are somewhat

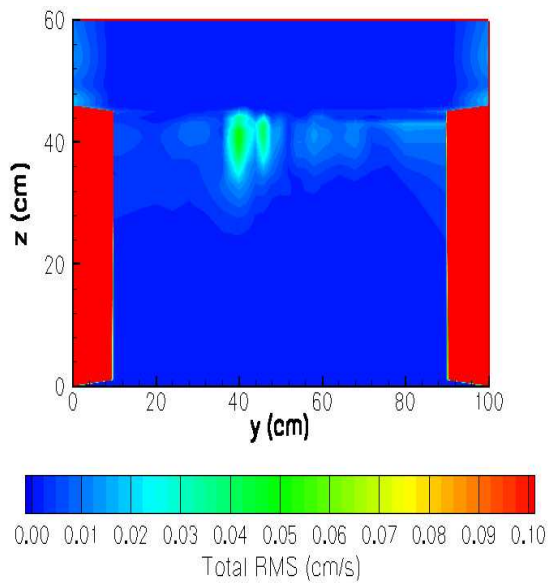

Figure 3–4: 3D effects captured by TRUCHAS experimental simulations, with the total rms deviation from the mean velocity displayed in a cross-tank view at x = 220 cm along the tank. The exclusion of boundary nodes in the variance calculations is evidenced by the blanked values at the tank sidewalls.

disappointing given the relatively high values of mean velocity of close to 95 cm/s focused within the crest of the wave. It is our belief that higher resolution would better capture small scale turbulent structures and thus significantly effect these values, a hypothesis that is further explored in the following chapter.

CHAPTER 4
RESULTS

4.1 Wave Focusing and Breaking Dynamics

It was our aim to provide a model competent in the simulation of realistic wave breaking events. Ideally, this model would accurately capture the detailed and complex flow characteristics inherent in wave generation, propagation, focusing, and breaking. Even more so, a superlative model should be able to represent such important breaking aspects as turbulence generation and eddy formation. A more in-depth look into the model simulations and capabilities is given in the following subsections.

4.1.1 Breaking Visualizations

Initial reports from the laboratory experiment we strove to simulate indicated that a spilling breaker occurred within the 3 m section between measurement locations A and B. A composite of Particle Image Velocimetry (PIV) images of the surface of the spilling breaker, as provided by Donelan and Haus, is given in Fig. 4–1. Successive

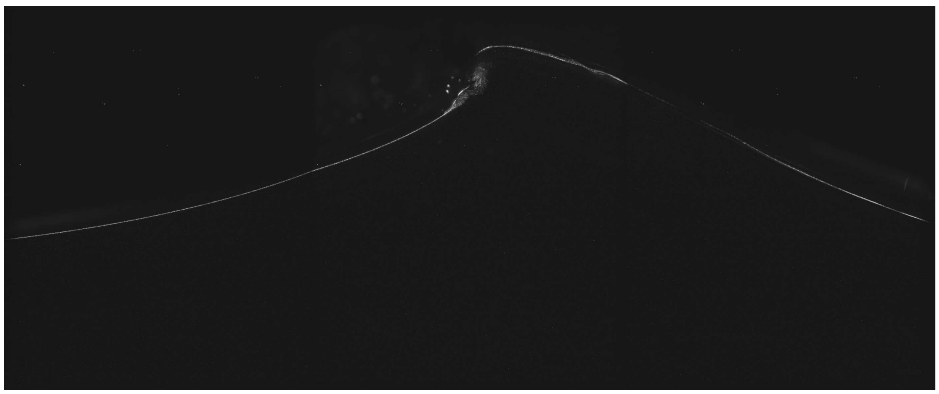

Figure 4–1: A composite of PIV images for the laboratory spilling breaker.

laboratory runs dictated this spilling breaker to be highly repeatable under the same experimental conditions. Subsequently, it was our hope that TRUCHAS would accurately capture these detailed breaking conditions, and that such a spilling breaker

would be the realization of our numerical efforts. Breaking, unfortunately, does not readily make itself apparent within the visual aspects of our model simulations.

Fig.4–2 contains a snapshot of the steepest wave profile obtained for our model simulation, including a closer view of the wave of interest.[1] While the wave packet

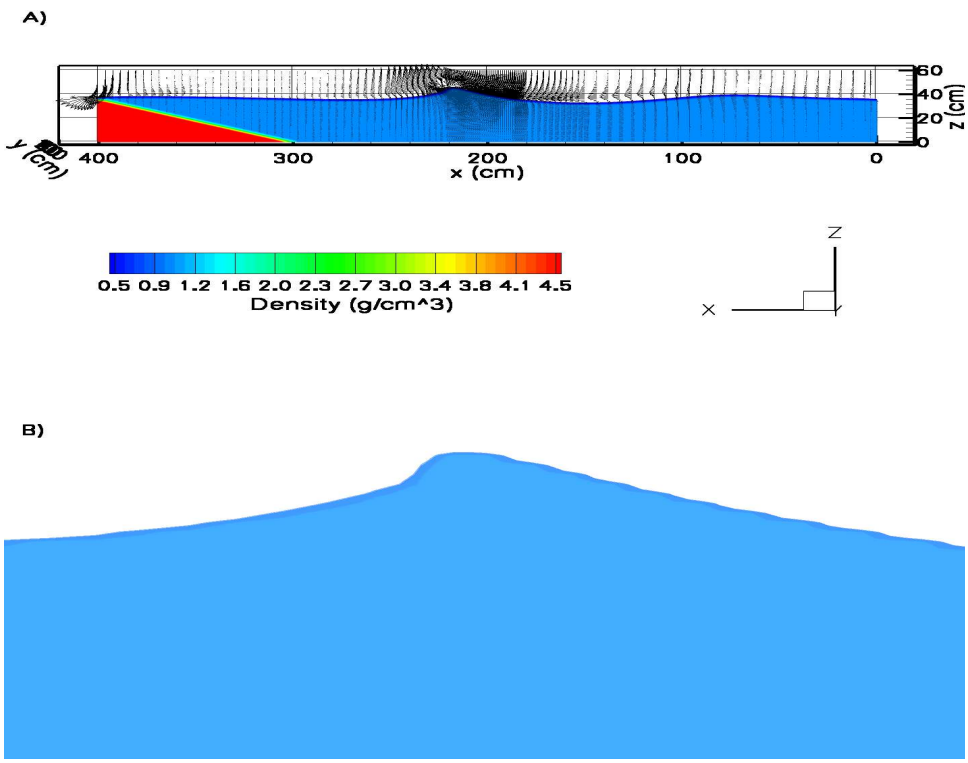

Figure 4–2: A snapshot of the flow visualization at the critical point in the numerical simulation. A view of the entire numerical tank is given in A), with a closer view of the focused wave at its steepest point in B).

has successfully focused to create a steep waveform seemingly on the threshold of breaking, there is little visual evidence to suggest that the wave actually overturns. A closer view of the wave of interest is given in Fig. 4–3. A 1:1 ratio between x and z axes is maintained in this figure, and the grid has been partioned to facilitate

[1] Note that the tank profile depicted in A) is drawn with an exaggerated z-axis such that the profile might readily fit within the viewing window. The plot shown in B), however, retains a 1:1 aspect ratio.

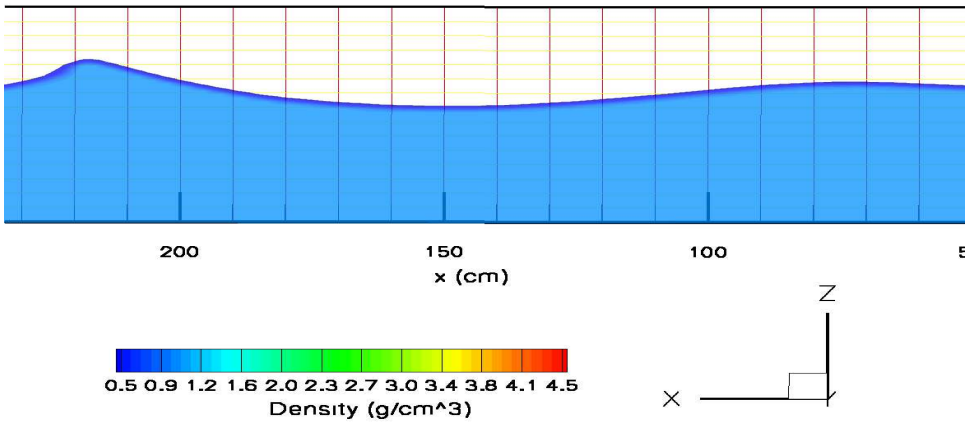

Figure 4–3: A closer view of the steep wave of interest.

calculations of wave steepness. The red lines mark every 10 centimeters in the x-direction, and the yellow lines are representative of 4 cm spacing in the vertical direction. As indicated in Dean and Dalrymple (2002), waves break in deep water due to excessive energy input, resulting in a breaking wave steepness of H/L $\approx$ 1/7. From the grid displayed in Fig. 4–3, we can establish a wave steepness of approximately 0.1. Hence, it would appear that our wave of interest does not steepen sufficiently to warrant a breaking episode. Still, a more in-depth analysis of the wave characteristics is warranted.

4.1.2 Mean Velocity

The velocity field under a progressive wave is an important factor to consider in determining the accuracy of a model to depict wave development and breaking. Via the methods outlined in Section 3.3.3, a mean velocity field was extracted from the model results. Fig. 4–4 is a depiction of the mean velocity field corresponding to the critical point, when the “breaking” wave is at its steepest position. The mean velocity field depicted in Fig. 4–4 is an encouraging justification that TRUCHAS appears to be performing well in propagating and focusing the waves in a realistic manner. As one

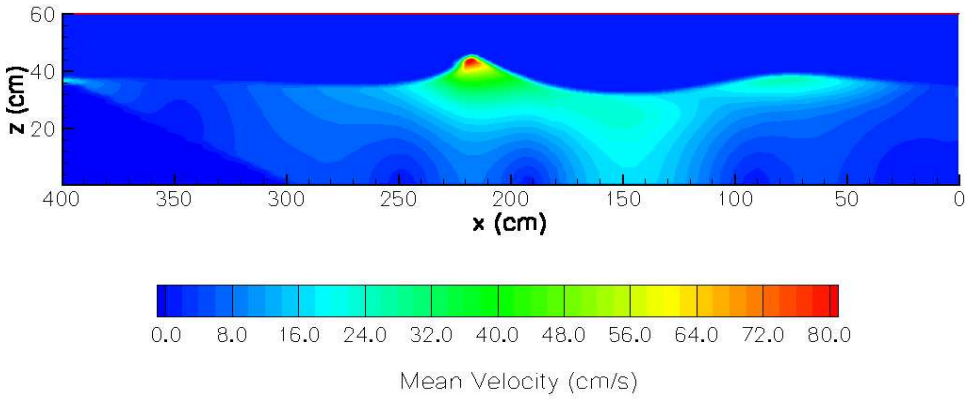

Figure 4–4: Cross-tank averaged mean velocity field at the critical point of the simulation, corresponding to time t = 4.47 seconds.

would expect for a wave approaching the breaking point, velocities at the crest of the steepening wave are high, with values nearing 95 cm/s. These intense velocities also seem to be impinging on the forward face of the wave crest, suggesting a wave front that is very near spilling.

It is also encouraging to note that the majority of the mean velocity at the crest and trough locations is reflective of high *u* velocities in this region, whilst the vertical velocities are nearly zero at this point as one might expect for a realistic progressive wave. Phase speed estimates for the critical wave were found to be approximately 90 cm/s. The slightly higher horizontal velocities in the crest in comparison to the phase speed of the wave is a promising indication that the critical wave is steepening toward breaking. In addition, a group velocity for the wave train can be obtained via Eq. 4–1, taken from Dean and Dalrymple (1991).

$$Cg = nC = \frac{C}{2}(1 + \frac{2kh}{sinh(2kh)}) \tag{4–1}$$

where
$Cg =$ group velocity

C = wave celerity
k = wave number
h = water depth

Utilizing the wave period of 1 second and a water depth of 36 cm, a wave number of $0.04386\mathrm{cm}^{-1}$ is obtained. This information, in conjuction with the phase speed of 90 cm/s found above, gives rise to a group velocity of 57.1 cm/s. Such velocity values are in accordance with wave group theory in intermediate and deep water, in which the individual waves travel faster than the wave packet. As such, waves will propagate through the wave packet over time, and the results presented hereafter will substantiate this claim.

Fig. 4–5 shows the time series for horizontal velocities at the location along-tank at which the critical wave reaches it steepest point, x = 220 cm. So as to produce a

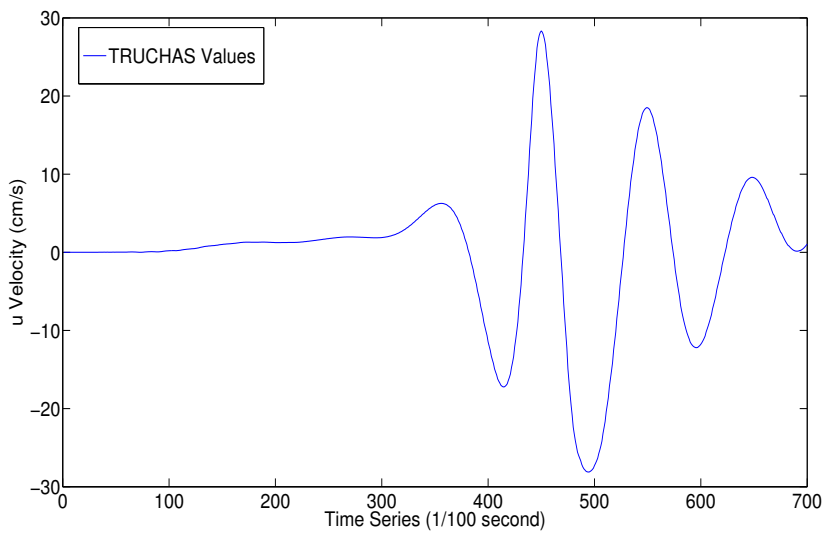

Figure 4–5: A time series of the horizontal velocities at the expected breaking point of the wavetank (x = 220 cm).

smooth velocity time series, velocity calculations reflected in this plot were taken at a vertical height of z = 29 cm. As such, the horizontal velocities are not representative of those at the free-surface and are therefore lower than the highest expected velocities at this point. Although there is no laboratory data, of yet, with which to compare

Fig. 4–5, it is evident that the wave of interest retains the highest horizontal velocities as it passes the critical point and is followed by a subsequent wave with lower *u* velocities. It is of interest to note that, in accordance to the group and phase velocities outlined above, the critical wave has propagated to the front of the wave packet from its previous position in the wave group, as was shown in Fig. 3–3. In similar fashion to the high *u* velocities shown in the crest of the wave in Fig. 4–4, the points midway between crest and trough represent mainly *w* velocity values, which can be as great as 40 cm/s. True to laboratory waves in intermediate and deep water, orbital velocities within our model waves also diminish with depth, as can be seen in Fig. 4–4. Such results substantiate the claim that TRUCHAS is performing well on fundamental levels.

4.1.3 RMS Velocity

A tell-tale sign of wave breaking dynamics is turbulence production. One way to quantify the turbulent kinetic energy being imparted into the water column is to view the total rms deviation from the mean velocity, as detailed in Section 3.3.3. Great variance from the mean velocity in the area of expected breaking would suggest turbulence generation in this region, an indication that some form of breaking is occurring. The total rms deviation from the mean velocity for our simulations, averaged across the tank, is given in Fig. 4–6.

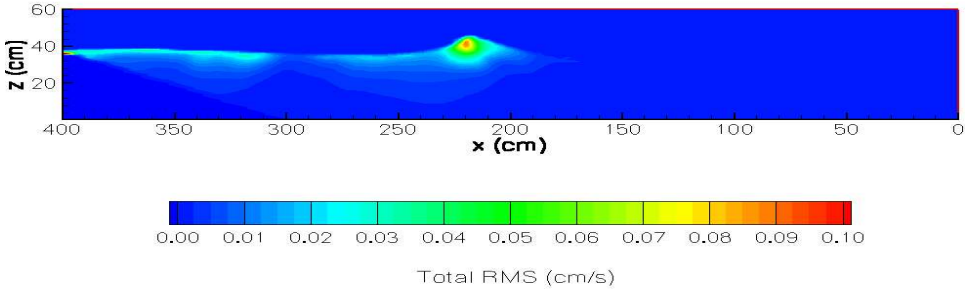

Figure 4–6: Total rms deviation from the mean velocity at the critical point of the simulation. Time is 4.47 seconds into the simulation.

While there is evidence of a variation in velocity across the tank at the critical point, the values indicated in Fig. 4–6 are disappointingly low, with total rms velocity values only reaching 0.1 cm/s. As explained by Pope (2000), the largest turbulent eddies to be produced by a system are comparable in length, velocity, and Reynolds number to that of the flow scale. According to the energy cascade, these large eddies become unstable and break up, imparting their energy into smaller eddies. This process is continued until the smallest eddies are stable and molecular viscosity is efficient in dissipating kinetic energy. Consequently, the disturbingly small values obtained for total rms velocity dictate that there is not substantial turbulent eddy production occurring within the flow dynamics. These values are, in fact, over an order of magnitude smaller than what would be considered relevant turbulent velocities.

As discouraging as these results may be, not all hope is lost for the possibility of a breaking event in model simulations. The smallest resolvable turbulent structures that can be modeled in a simulation are those no less than 2 grid cells wide. Hence, with a grid spacing of 2 cm at its finest in the cross-tank direction, we may be missing many turbulent structures that are indeed inherent in our "breaking" wave, indicating that there are many more parameters to consider in the analysis of our model's predictive capabilities. Model simulations are compared to laboratory results in the following section to further define the capabilities of TRUCHAS in predicting wave breaking events. The possibility that breaking may be occurring unbeknownst to the users due to such factors as inadequate resolution are also addressed in subsequent sections.

4.2 Comparison to Laboratory Data

The successful wave model should demonstrate an ability to accurately recreate laboratory experiments, and consequently to provide the user with results similar to those measured in a laboratory environment. The validation of our model to readily and accurately depict wave focusing and breaking events is dependent upon laboratory results as provided by our partners in Miami. The results provided by Donelan and

Haus serve as a comprehensive means by which to verify the success of our model. Model-laboratory comparisons for a variety of flow parameters are considered in the following subsections.

4.2.1 Horizontal Velocity

As was described in Section 3.1, laboratory measurements of the free-surface elevations were taken at two locations within the ASIST. Values for horizontal and vertical velocities at even increments below the free-surface were then acquired via the methods outlined by Donelan *et al.* (1992). The data retained from the first location, that of location A, was manipulated and used as the forcing for our model simulations. The data obtained at location B, approximately 3 m from the forcing boundary and after the breaking region, serves as a means by which to evaluate the model data after breaking.

Fig. 4–7 shows both the laboratory results and those calculated by TRUCHAS at point B. As with the time series comparisons for location A given in Subsection 3.2.2, it should be noted that data for both laboratory and model velocities was calculated at a cross-tank location of y = 50 cm and a vertical location of z = 29 cm to ensure a continuous time series plot. The laboratory values for horizontal velocity possess greater fluctuations in the early stages before the larger waves reach the measurement location. This can be attributed to the fact that the free-surface laboratory measurements, and corresponding velocity calculations, were taken over a 20 second interval. Model simulations, on the other hand, were forced with the middle 7 seconds of the laboratory data set, where the larger waves, and main constituents of the wave packet, are generated and propagate to breaking.[2] This method allowed us to save on

[2] A test simulation was also conducted utilizing the full 20 seconds of laboratory data. Visual analysis suggested no difference between run results for the 20 second and 7 second simulations. The 7 second data set was therefore employed for final simulations due to its significantly smaller computational run time.

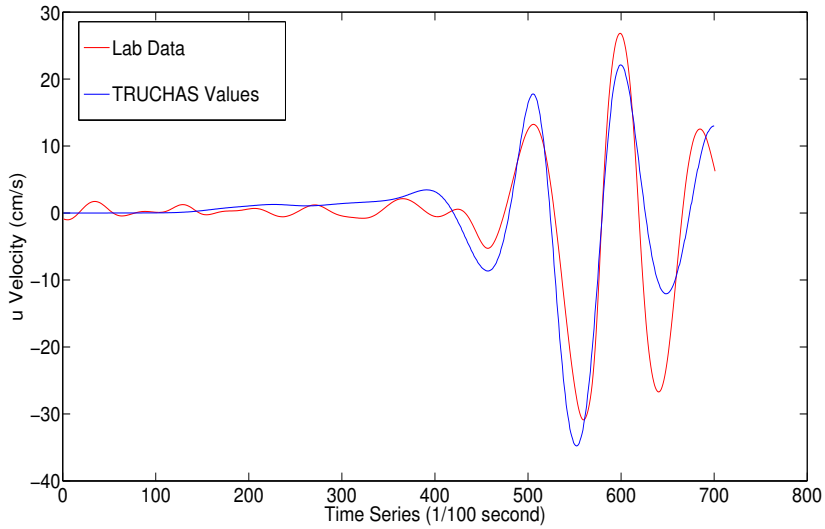

Figure 4–7: A comparison of horizontal velocities calculated for the laboratory experiment and those predicted by TRUCHAS. Model measurements are taken at approximately 3 m from the forcing boundary. The earliest waveform depicted on the plot is that of the "breaking" wave.

computational time while still maintaining the major components of the focusing wave packet, and is ultimately a reason that model velocities are smaller than those recorded in the laboratory for the early stages of wave propagation.

As the larger waves propagate through the point of interest, it is apparent that our model overestimates the u velocities in both the crest and trough of the wave of interest (that represented by the first waveform in Fig. 4–7) by nearly 5 cm/s. In addition, a phase difference between the laboratory data and the model data becomes apparent after the critical wave passes the plane of view. These observations point to the visual claims made earlier that the model wave does not appear to break as we had initially anticipated that it would. The fact that the horizontal velocities for the model wave are approximately 5 cm/s higher than those for the laboratory wave indicate that the model wave did not break in a manner similar to that realized in the laboratory setting, as explained below.

It has been well-documented that turbulent flow fields produce highly variable velocity fields that can fluctuate substantially on a rapid time scale. A velocity field $U(x,t)$ can be decomposed into its mean, $< U(x,t) >$ and fluctuating, $u(x,t)$, parts such that $u(x,t) \equiv U(x,t) - < U(x,t) >$ (Pope, 2000). This fluctuating velocity can drive turbulent eddy formation, as well as act to hinder the progress of the initial waveform. Pope (2000) clarifies this phenomenon through an examination of a form of the Reynolds Equations, given in Eq. 4–2.

$$\rho \frac{\bar{D} < U_j >}{\bar{D}t} = \frac{\partial}{\partial x_i}[\mu(\frac{\partial < U_i >}{\partial x_j} + \frac{\partial < U_j >}{\partial x_i}) - < p > \delta_{ij} - \rho < u_i u_j >] \qquad (4\text{–}2)$$

where
$< U >=$ mean velocity field
$\frac{\bar{D} < U_j >}{\bar{D}t} =$ rate of change of the mean velocity following a point moving with the local mean velocity; also known as the mean substantial derivative of the mean velocity
$\rho =$ density
$\mu(\frac{\partial < U_i >}{\partial x_j} + \frac{\partial < U_j >}{\partial x_i}) =$ viscous stress term
$- < p > \delta_{ij} =$ isotropic stress derived from the mean pressure field
$-\rho < u_i u_j >=$ turbulent shear stress arising from a fluctuating velocity field

Convention permits $< u_i u_j >$ of the turbulent shear stress term in Eq. 4–2 to be labeled the Reynolds stress. This Reynolds stress stems from momentum transfer as a result of the fluctuating velocity field inherent in turbulent flows. As Munson *et al.* (2002) points out, the turbulent shear stress, $-\rho < u_i u_j >$ takes on a positive value for turbulent flows, thereby causing a greater shear stress in turbulent flows as opposed to laminar flows. A natural increase in turbulent kinetic energy, defined as $\frac{1}{2}$ the Reynolds stress tensor or $\frac{1}{2} < u_i u_j >$, would also ensue. The resulting flow response is a decrease in the mean velocity field with axial distance into the flow regime, coupled with a spreading out, or mixing, of the flow field.

Wave breaking being a very nonlinear and certainly turbulent process, we would expect this response in the laboratory waves, and results seem to validate this assumption. The physical laboratory's steep wave event has already resulted in a

spilling breaker once it reaches point B. Thus, much of the kinetic energy associated with the wave has gone into turbulence and eddy formation, and the fluctuating velocity field is greatly increased. The resulting high Reynolds stresses act to decrease velocities in the laboratory waveform, thus allowing the subsequent waves to overtake this wave. As a result, there is an initial phase lag between the model and laboratory waves, as the laboratory wave experiences a slowing due to turbulence production. However, as the subsequent waves overtake the breaking laboratory wave, energy may be fed into these waves, and their velocities increased.

The initial model wave retains the majority of its energy and does not see much turbulent dissipation. As was indicated in Fig. 3–4 of Chap. 3, model velocity fields show little variability in the cross-tank direction. Consequently, there is little in the way of a fluctuating velocity field to incur substantial Reynolds stress values and slow the waveform. Subsequent model waves, therefore, are not afforded the opportunity to overcome and feed off of this wave. As such, velocities in the waves following the "breaker" are lower than those in the laboratory, and the model waves are then seen to lag the laboratory waves for waveforms following the initial breaker. Having received less energy from the preceding waves, model waves are continually damped by the numerical smoothing, and do not see the same increase in energy and velocity experienced by the laboratory waves.

A view of the mean velocity field at point B is given in Fig. 4–8. In contrast to Fig. 4–4, which depicts large velocities in the crest at the steepest point in the wave evolution, Fig. 4–8 shows much smaller crest velocities at point B, nearing only 30 cm/s. This plot is included as verification that the horizontal velocities within the wave of interest have been significantly reduced from those seen at the steepest point in the simulation, and that the first wave form in Fig. 4–7 is indeed the critical model wave that was expected to break. The reader is reminded, however, that velocities displayed

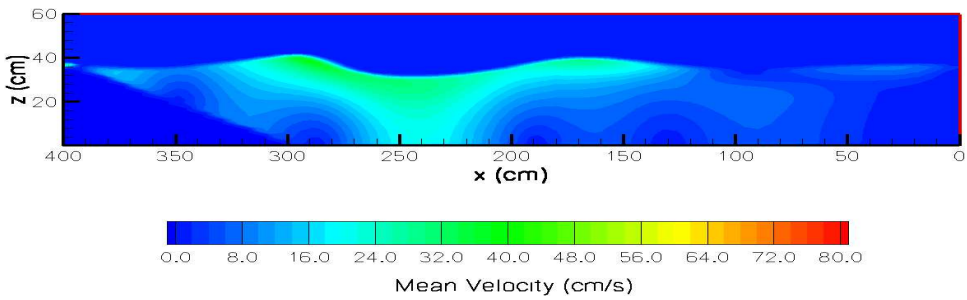

Figure 4–8: The mean velocity field at location B, as calculated by TRUCHAS.

in Fig. 4–7 are slightly lower than the highest expected crest values, as the calculations are conducted at a vertical height of 29 cm above the bed and not at the free-surface.

4.2.2 Vertical Velocity

A similar pattern as that reported above for horizontal velocity is seen within model-laboratory comparison for vertical velocities. As shown in Fig. 4–9, increased vertical velocities of close to 5 cm/s are depicted in the “breaking” wave simulated by TRUCHAS, as compared to the laboratory breaker. Vertical velocities in the model wave packet are then seen to underestimate laboratory calculations for the subsequent wave by over 5 cm/s, with a drastic underestimation of the negative vertical velocities of approximately 15 cm/s.

As illustrated in the previous subsection, a reasonable explanation for this dissimilarity again seems to fall upon to the failure of the model to successfully produce a spilling breaker. Given the substantial evidence supporting the fluctuating velocity field inherent in turbulent flows, it seems likely that the spilling breaker produced in the laboratory setting would impart much of its kinetic energy and momentum into the water column, spawning turbulent eddies. The increase in turbulent

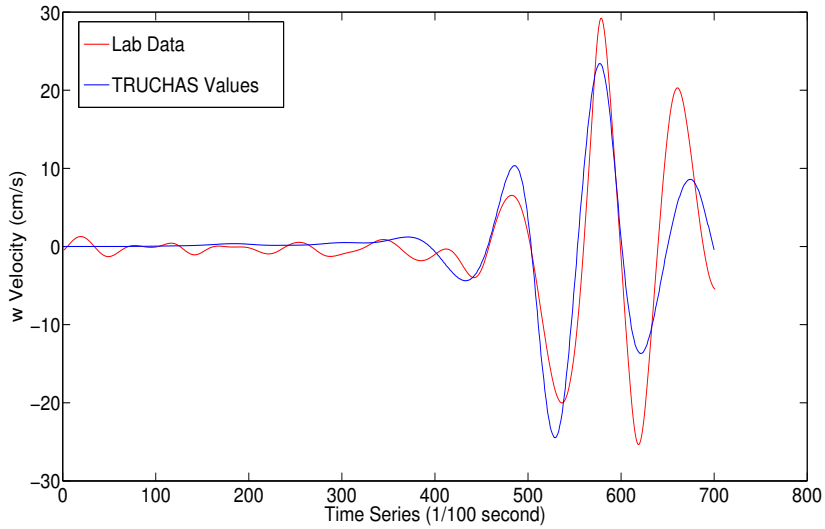

Figure 4–9: A time series of both laboratory and simulated vertical velocities. Model measurements are taken at point B, approximately 3 m from the forcing boundary. The wave of interest is represented by the preliminary waveform.

kinetic energy, with a corresponding increase in Reynolds stress, would then act to deter the speed of the wave, allowing subsequent waves to overtake the breaker, thus steepening the waveforms and intensifying wave characteristics. The phase lag experienced by the laboratory breaker but not the model wave of interest is further evidence to this end, an explanation for its occurrence being detailed previously.

Although discouraging that the model results differ significantly from those found in ASIST, it is heartening to see that the *u* and *w* velocity profiles for TRUCHAS waves show similar characteristics and trends. This indicates that the tendency away from breaking of these model waves is the result of some underlying dynamics being experienced by TRUCHAS waves, and not necessarily by errors within individual velocity calculations. Further verification of this finding can be found in the comparison of the free-surface displacement, analyzed in the Subsection 4.2.3.

4.2.3 Free-surface Displacement

Model results for free-surface displacement follow the same trend seen in the time series for horizontal and vertical velocities, examined above. The free-surface elevation

for the model was calculated from the pressure field at location B as generated during a TRUCHAS simulation. A short program was developed to extract the vertical cell location containing the free-surface for each time step at location B, based on the pressure values for each cell, as shown in Eq. 4–3, taken from Dean and Dalrymple (1991).

$$P = -\rho g z + \rho g \eta k_p(z) \tag{4–3}$$

where
$P =$ pressure
$\rho =$ density
$z =$ vertical position, taken as zero at the free-surface
$\eta =$ free-surface elevation
$k_p(z) = \dfrac{coshk(h+z)}{cosh(kh)}$
Thus, the pressure field calculated by TRUCHAS can be manipulated to obtain a value for η at location B for every time step of the simulation, which can then be correlated to measurements taken during laboratory experiments.

Fig. 4–10 shows the time series of free-surface displacement, η, at location B for both model and laboratory results, the mean water level having been removed. The continuous pressure field modeled by TRUCHAS produces the smooth free-surface elevation time series shown in Fig. 4–10. In contrast, the laser method used in the laboratory setting is seen to produce a very detailed plot, with the ASIST's free-surface elevation exhibiting a complex and varied signature. It is also worthwhile to remind the reader that model simulations were forced with the middle $\frac{1}{3}$ of the laboratory data for location A, thus early model calculations for η do not reflect the same variability, and the small-scale fluctuations present in the laboratory data during this time period are subsequently not captured in the model. To verify the free-surface elevation obtained from the model's pressure field, a program was written in which the volume of fluid (VOF) field was used to calcuate the free-surface elevation. The VOF field was utilized to determine the vertical location of the water surface at each time step, and the mean water level was removed to produce free-surfaces accurate to within 1 centimeter. As

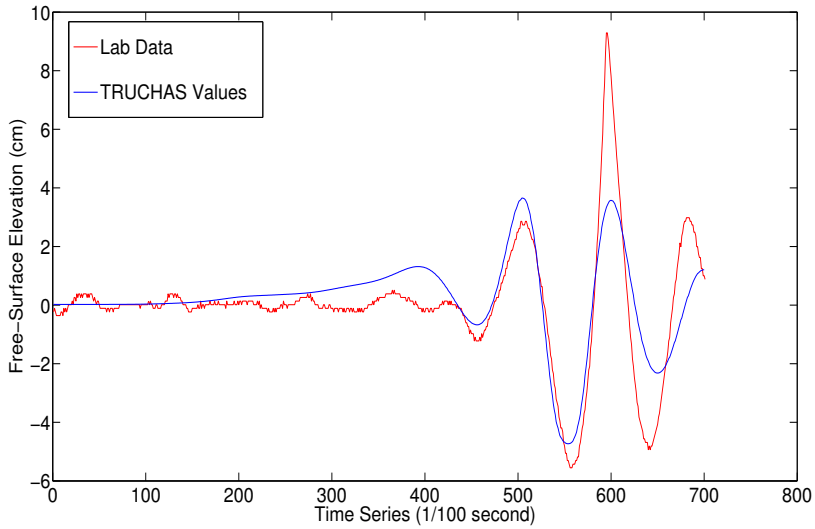

Figure 4–10: A time series of the free-surface displacement as calculated by TRUCHAS at location B and its comparison to laboratory measurements. Free-surface elevation is reported in cm with mean water depth removed. The initial waveform represents the "breaking" wave of interest.

the VOF field is not continuous but rather is a series of point-values calculated within each grid cell, the resulting free-surface elevation time series was given a rather choppy appearance. The overall plot, however, very closely matched that obtained via the pressure field method.

In concurrence with the pattern noted in Figs. 4–7 and 4–9, Fig. 4–10 depicts a taller wave of interest in model results than that measured in the laboratory. The higher crest elevation of the initial waveform again gives credence to the hypothesis that the model wave steepens but does not undergo breaking, rather devolving back into a more stable waveform. In addition, TRUCHAS, once again significantly underpredicts the characteristics of the subsequent wave, missing the peak elevation by a magnitude in excess of 6 cm and the trough by nearly 3 cm. Of interest to note is the nearly identical free-surface elevations attributed to both the model wave of interest and that of the following wave. This gives the appearance of a more uniform wave train, and seems to suggest that in lieu of breaking, the steep wave event has instead receded

to form a more stable, uniform wave packet configuration. This implication will be revisited in Section 5.4 of our discussion.

As alluded to in the previous section, the comparison illustrated in Fig. 4–10 serves to further validate the adopted hypothesis that the model waves do not respond in the same manner as those produced in ASIST. The correlation between high free-surface elevation and high velocities in the initial waveform, followed by a drastic decrease in elevation and velocities in the second waveform is encouraging, indicating that the underlying factor preventing the spilling of the model waves is manifested in all of the flow fields produced by TRUCHAS, from VOF to pressure to velocities. In addition, the same phase lags between model and laboratory measurements are present in all of the velocity and η plots presented. As such, it does not appear as though there is a distinct problem with the forcing mechanism for TRUCHAS, created by the authors of this study, but rather a tendency toward nonlinearities inherent in the flow computations of the model that are producing such a result. Still, the dependence on user input to successfully model breaking has not been closely examined. The subsequent section is dedicated to this analysis.

4.3 Sensitivity to User Input Specifications

Given that the model results are not as close to the laboratory results as we would have hoped, we began to question the model's sensitivity to user-specified flow dynamics. Questions arose as to the benefits of such specifications as the turbulence model and increased grid resolution in more accurately resolving the turbulent structures we had expected to reproduce. To ascertain the validity of these options, test cases were conducted to examine each user input individually.

4.3.1 Turbulence Model

As was mentioned in Chap. 3, initial test cases seemed to suggest that the algebraic turbulence model was unnecessary in successfully simulating the laboratory investigation. The inability of the TRUCHAS model to resolve small-scale turbulent

structures, however, caused us to reconsider the stance previously taken. As such, a new simulation was designed to mirror the simulations specified above, with the simple change of activating the algebraic turbulence model, detailed below. Fig. 4–11 shows the u and w velocities given after breaking for both runs, with and without the turbulence model. The velocity profiles shown in Fig. 4–11 are nearly identical,

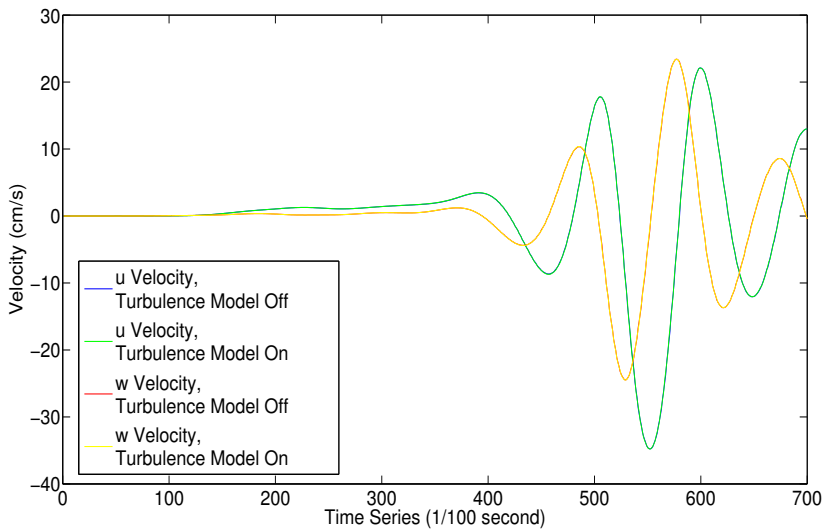

Figure 4–11: Horizontal and vertical velocity profiles at point B, 3 m downstream of the forcing boundary.

indicating that the orbital velocities seem to be little affected by the presence or absence of the turbulence model. This result is consistent with the findings mentioned in Chap. 3, where it was deemed that the algebraic turbulence model did little to improve the dynamics of the flow field.

A more detailed comparison is provided in Fig. 4–12 and Fig. 4–13, which show the differences in the results of this new run and model results without the turbulence model invoked. Consistent with the findings mentioned above, the comparison of Figs. 4–12 and 4–13 indicate that the mean velocity fields for both runs are almost identical. As such, the large scale dynamics associated with the generation and focusing of the wave packet are nearly indistinguishable for both cases.

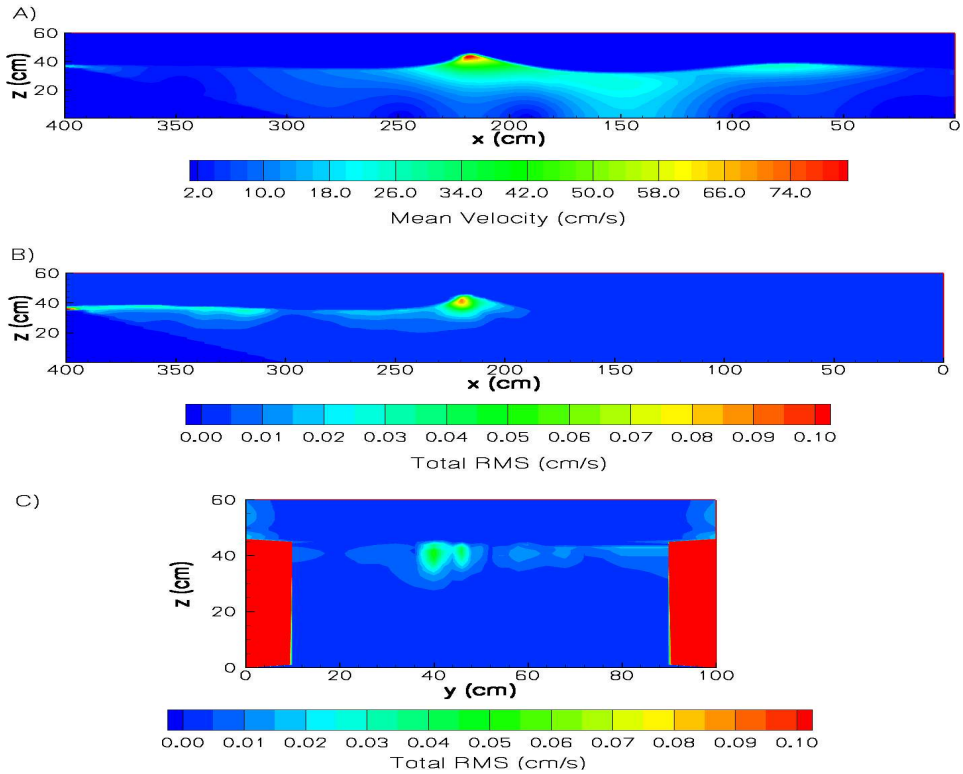

Figure 4–12: Model results for mean velocity and total rms without the algebraic turbulence model. The mean velocity is presented in A), while along-tank and cross-tank depiction of total rms are given in B) and C), respectively. Snapshots are taken at the critical point in the simulation, corresponding to 4.47 seconds.

However, upon closer examination of the breaking region, detailed in B) and C) of Figs. 4–12 and 4–13, we do find slight discrepancies between simulations. In the study involving the algebraic turbulence model, we find slightly smaller total rms values within the wave crest, as well as less variation in the cross-tank direction. Total rms values for both simulations, however, are still very small. Thus, there seems to be no distinct advantage, save computational time, to using one method over the other. In fact, it seems most fitting in order to facilitate increased turbulent production in the simulations to neglect the algebraic turbulence model, as this acts only to further dampen any eddy structures that may be forming.

The simplicity of the algebraic turbulence model included in TRUCHAS may be an underlying reason behind the poor numerical results given when this model is

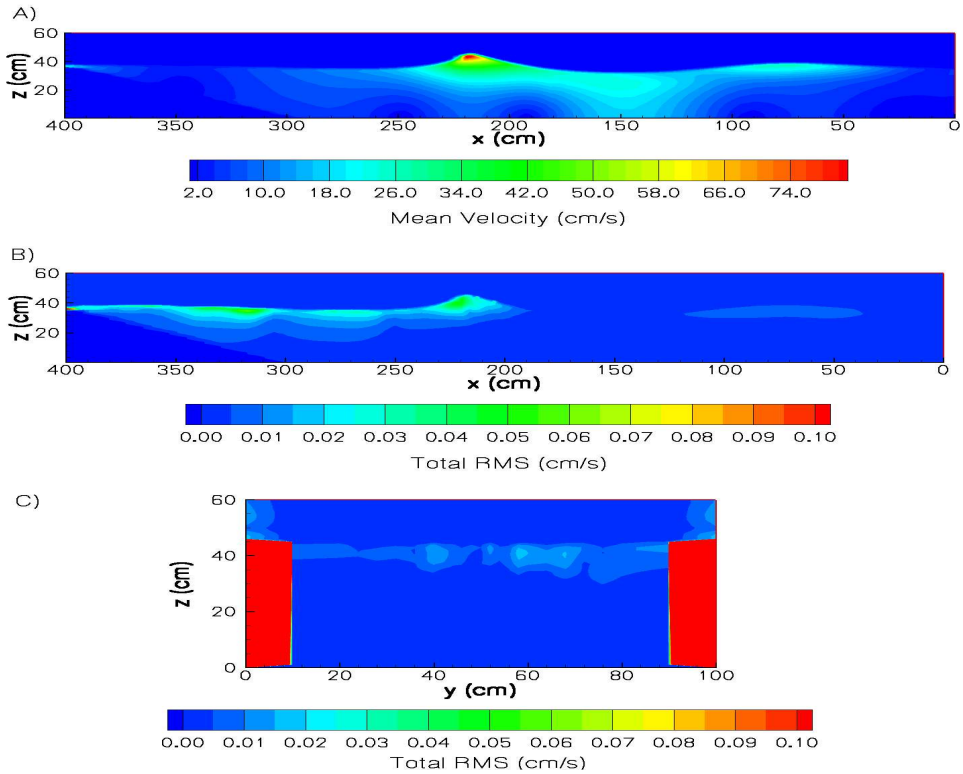

Figure 4–13: Model results for mean velocity and total rms with the algebraic turbulence model invoked. Again, mean velocity is shown in A), while plane and cross-section views of total rms are provided in B) and C), respectively. Snapshots are taken at the critical point in the simulation, corresponding to 4.47 seconds.

invoked. This turbulence closure model involves the simple calculation of turbulent diffusivity as outlined in Eq. 4–4.

$$\nu_T = C l_m \sqrt{\frac{1}{2} K U^2} \tag{4–4}$$

where
ν_T = turbulent diffusivity
C = proportionality constant between the turbulent diffusivity and the product of the turbulent length and velocity scales
l_m = mixing length, chosen to represent the size of the turbulent eddies
K = fraction of mean flow kinetic energy that is assumed to give rise to the turbulent kinetic energy
U = mean flow velocity

The effectiveness of the algebraic turbulence model relies on complete knowledge of the flow geometry, as C, l_m, and K are all terms specified by the user at the onset

of the simulation. [3] Pope (2000) warns that for complex flows for which turbulent mixing lengths are variable or unknown, the user specification of these parameters is mainly guesswork, and can lead to erroneous results. Hence, the default values that were used in our simulations may be problematic, and a separate investigation into the most effective constants for this simulation is warranted before a definitive statement as to the effectiveness of the model's algebraic turbulence model can be made.

4.3.2 Increased Resolution

Arguably the most important feature to consider when trying to resolve small turbulent structures is the mesh grid spacing. As mentioned previously, the smallest resolvable turbulent eddies are those no smaller than 2 grid cells in length. Accordingly, we have concern that the 2 cm grid resolution used in the cross-tank, or y-direction, may be a limiting factor in successfully modeling the smaller-scale turbulence we would expect to see within the breaking region. A test case was therefore set up in which the grid resolution was increased to 1cm by 1cm by 1cm grid spacing within the breaking region. The simulation, henceforth referred to as Run 2, was conducted as those examined above, without the utilization of the algebraic turbulence model, and results were compared to those obtained in the previous runs.

Surprisingly, results for Run 2 were poorer than those obtained with the original mesh. Casual observance of the focused wave packet indicates a less-steep wave event than those previously noted. Fig. 4–14 shows a decreased horizontal velocity in comparison with velocities corresponding to the old mesh at point B. Though u velocities for the wave of interest corresponding to Run 2 still overpredict that of the laboratory data, at first glance there appears to be better agreement between the two.

[3] The proportionality constant, turbulent mixing length, and kinetic energy fraction designated in our simulations were the model default values of 0.05, 0.0254, and 0.1, respectively.

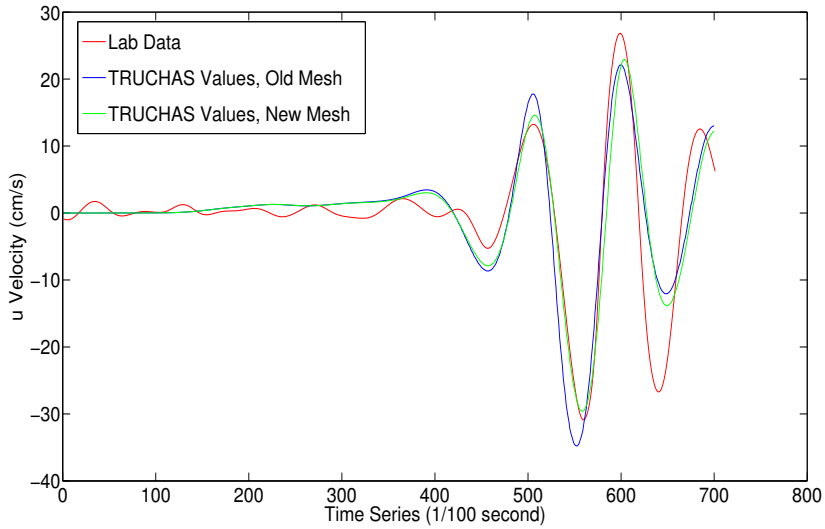

Figure 4–14: Resulting horizontal velocity time series for a new grid mesh taken at point B.

The phase lag that is apparent early on in Run 2 velocities, and that remains within the time series as subsequent waves cross the plane of view, however, gives cause for alarm. Despite the slightly higher u at the crest and trough of the wave of interest, the phase lag between the laboratory data and the model data after the passing of the first crest, prevalent in the old run profile, does not exist in the new mesh profile. Instead, the u velocity profile for Run 2 suggests that the initial higher velocities for the model wave allow the profile to briefly capture the laboratory results, but then immediately begin a continuous lag behind laboratory data.

Plots of vertical velocity and free-surface elevation, Fig. 4–15 and 4–16 respectively, for Run 2 show similar results. This would suggest that velocities in the new mesh profile are lower than that of the old not because of breaking, but rather are lower throughout the flow simulation in its entirety. The lower velocities for the wave of interest in Run 2 may also explain the slightly higher values for velocities and free-surface elevation in the crest and trough of the secondary wave. The high velocities of the first waveform in the old mesh are evident of a steeper, faster wave

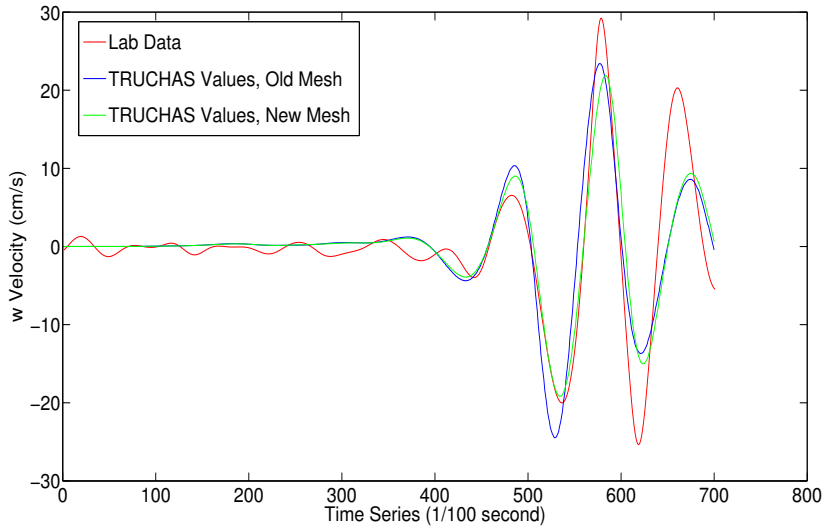

Figure 4–15: Resulting vertical velocity profile for a new grid mesh.

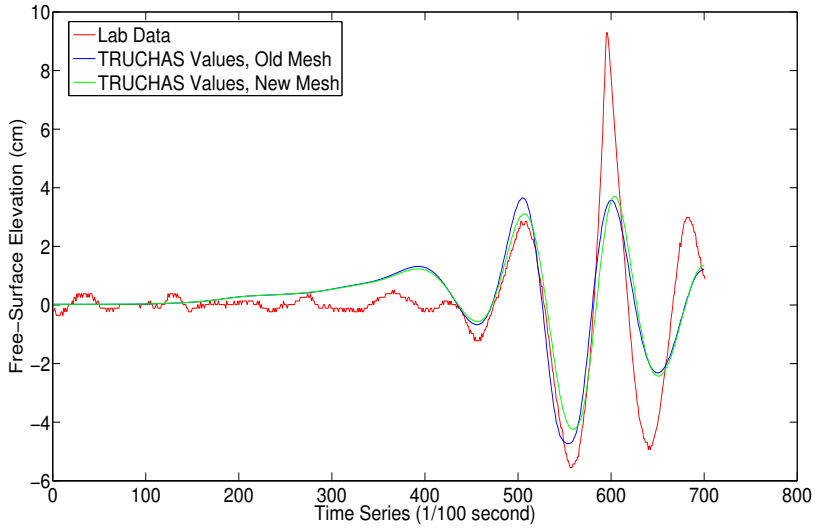

Figure 4–16: A comparison of free-surface elevations for Run 2 and those calculated with the original mesh.

passing the plane of view. Lower velocities in Run 2 profiles are indicative of the less steep, slower wave passing through. This slower moving wave may be slightly overtaken by subsequent waveforms, feeding them energy, and hence slightly increasing their velocities and free-surface displacements.

Thus, it appears that the critical wave generated in Run 2 has velocities everywhere in the domain less than that of the old mesh. This conclusion is verified in Fig. 4–17, which shows that the mean velocity at the critical point of the simulation, the same point examined earlier in Fig. 4–4, is drastically lower than that of previous runs, amounting to a mere 48.5 cm/s. The lower orbital velocities, and hence the

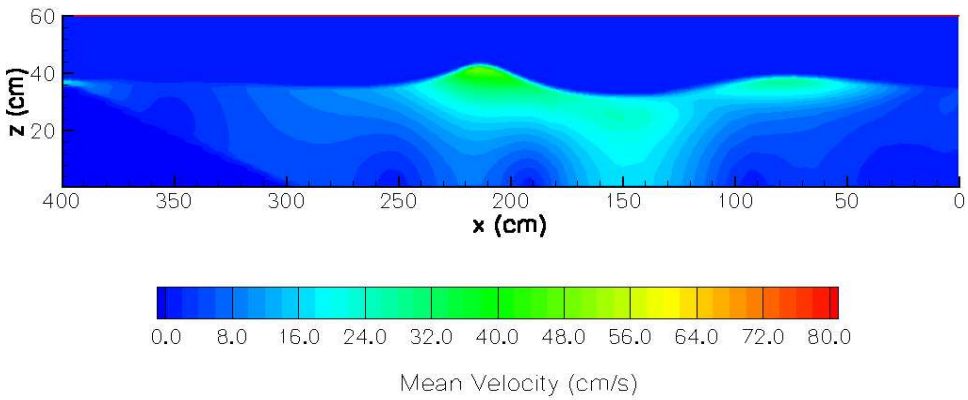

Figure 4–17: Run 2 results for mean velocity at the critical point of the simulation.

poorer results, of the new mesh simulation can be easily explained. While grid resolution was improved in the center of the mesh to 1 cm grid spacing in every dimension, grid cells had to be removed from the long-tank, or x, direction to save on computational time. Thus, grid resolution within the propagating region of the waveforms was reduced to as coarse as 9.6 cm grid spacing. Although not deemed a critical change at the time, it is not surprising that such coarse grid spacing would compromise the accurate resolution of the velocity field within this region.

A third and final mesh was therefore created to alleviate this problem and to provide more accurate results with which to assess the effect of resolution on turbulence production. Keeping the same scenario as utilized in the above runs, a simulation was performed with a third mesh and will be deemed Run 3. Resolution

was kept to 1 cm grid spacing in every dimension for the center of the breaking region, in similar fashion to that of Run 2. Grid cells were added to the x dimension, however, such that grid spacing within the propagation region was 4 cm resolution. This is an improvement over even the main runs focused on in this study, which contained a grid resolution of 6 cm in the propagation region. A sacrifice was consequently made in the post-breaking realm of the domain in that grid cells had to be removed from this region in order to increase resolution in the propagation region and still complete simulations in just over a week. Thus, grid spacing in the long-tank direction in this region was reduced to close to 9 cm resolution. A comparison of the along-tank and cross-tank clustering schemes used in the orginal run as well as Run 2 and Run 3 is given in Fig. 4–18.

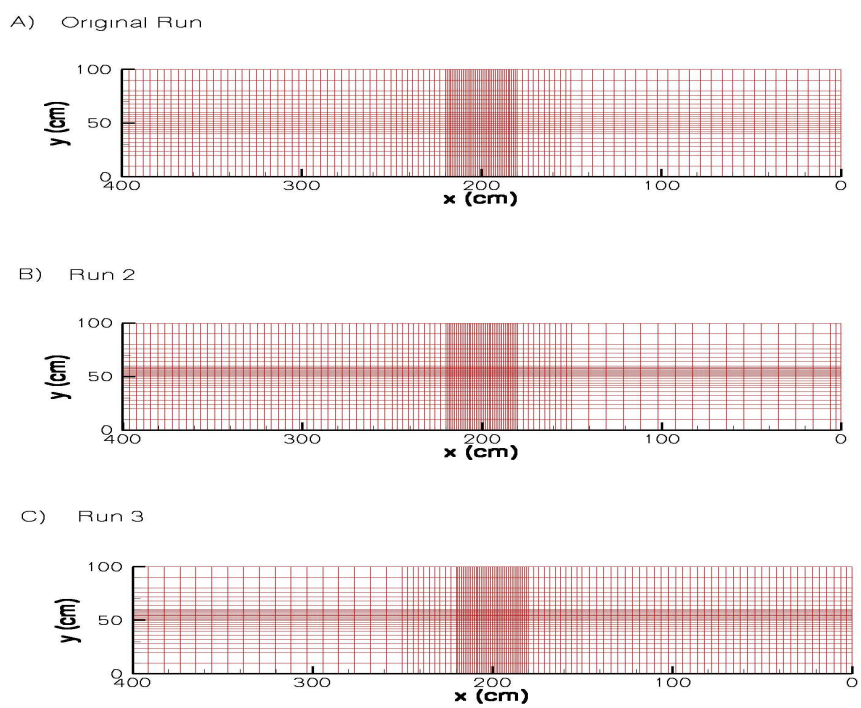

Figure 4–18: A comparison of the x and y clustering schemes utilized in all 3 simulations.

As evident in Fig. 4–19, the added grid cells in the propagation region of the computational domain did serve to improve the velocity field over that of Run 2. Though mean velocity values for Run 3 do not reach the magnitudes computed within

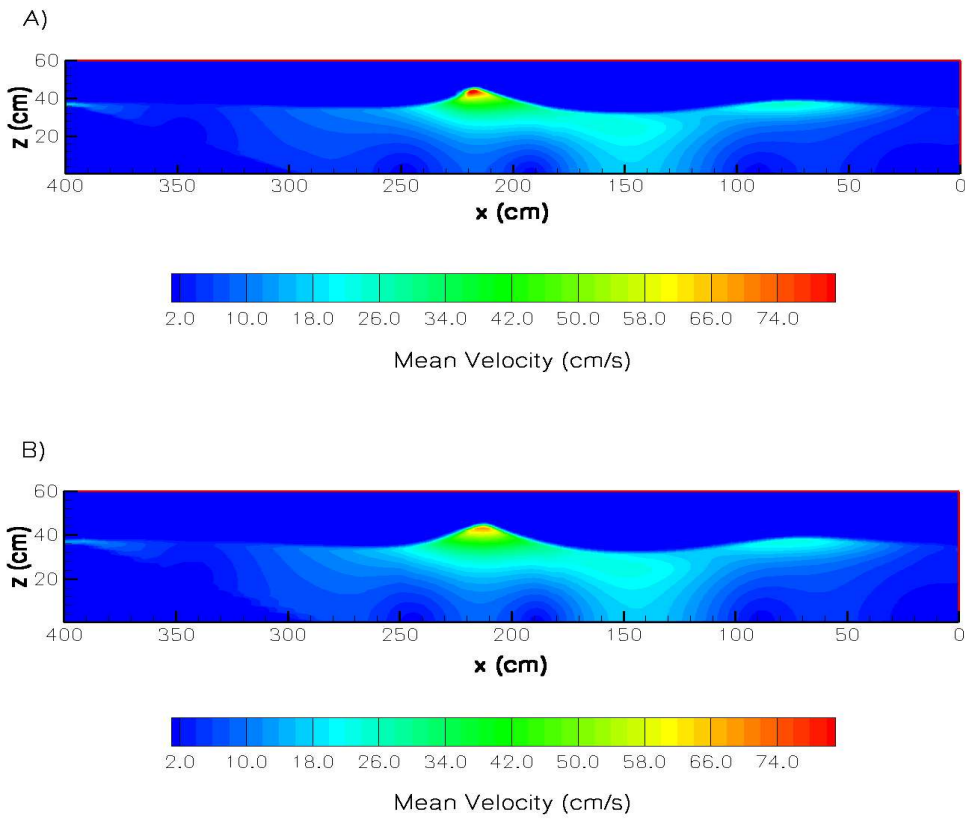

Figure 4–19: A comparison of the mean velocity field for the original simulation and that of Run 3. Mean velocity for original simulations is given in A), and that pertaining to Run 3 is shown in B). Both profiles are taken at the critical point in the simulations (t = 4.47 seconds), when wave velocities and steepnesses are greatest.

original simulations, mean velocities of 70 cm/s are captured within the crest of the critical waveform. The non-negligible increase in mean velocity values from Run 2 to Run 3 signify the importance of good resolution throughout the computational mesh. The addition of grid cells within the propagation region between Run 2 and Run 3 resulted in mean velocity values differing by over 20 cm/s. As is evident by these results, not only can small structures be easily overlooked in a grid lacking sufficient

cells, but erroneous flow fields may result from poor resolution, lending easily to flawed interpretations and invalid conclusions.

Also of interest in Fig. 4–19 is the form taken by each steep wave event. While the critical wave produced in original simulations has a highly nonlinear profile with a steep vertical face seemingly on the cusp of breaking, the critical wave of Run 3 has a more uniform appearance. The gentle forward face of this critical wave again seems to indicate a movement away from breaking and toward a more stable configuration. This result is surprising, as it was expected that the more finely resolved breaking region of the mesh utilized in Run 3 would provide a better indication of breaking than those of previous runs.

Despite the inclination of the critical wave away from breaking as substantiated by the mean velocity field generated in Run 3, improvements were seen within this simulation in the total rms deviation from the mean velocity measurements. Fig. 4–20 depicts the total rms field obtained via the methods outlined in Chap. 3 for the Run 3 simulation in comparison with that of the original runs. As indicated in the figure, total rms velocities more than doubled, to a value of 0.25 cm/s in the crest, for Run 3. While such values are still too slight to imply a breaking event, it is encouraging to note that a small increase in resolution, accomplished via the addition of only 5 cells to the cross-tank dimension, significantly improves the quality of our results.

Evident within this component of our investigation is the need to more efficiently resolve model computations in regards to computational time. Though many test cases were conducted early in the study to determine the most effective combination of such numerical parameters as courant number, convergence criterion, relaxation parameter, preconditioning steps, and maximum number of iterations, a closer examination of these details is warranted at this point in the model formulation. Any time that can be saved in the reduction of these parameters, while still accurately resolving flow dynamics, corresponds to grid cells that can be added to our domain without the

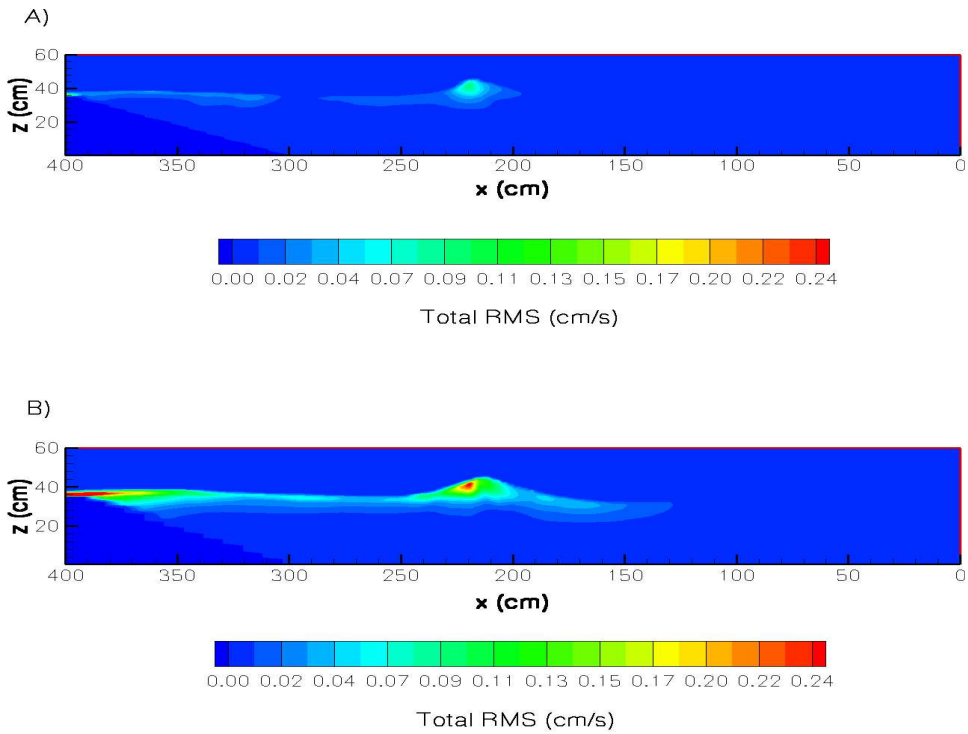

Figure 4–20: Total rms deviation from the mean velocity for original runs and that of Run 3. The total rms velocity field for original runs is given in A), while total rms values obtained with the more finely resolved mesh of Run 3 is shown in B). Measurements are taken at the critical point of the simulation, corresponding to t = 4.47 seconds

expense of increased simulation time. The manipulation of TRUCHAS to run in parallel, which thus far has proven unsuccessful on our available machines, will mark another huge step in the more accurate portrayal of the numerical wave packet. The elimination of the heavy restriction on grid resolution due to computational expense, which at this point is the limiting factor in our numerical model, would give way to more detailed flow simulations, possibly revealing flow dynamics that are present within our simulations but have yet to be realized.

4.4 Two-Phase Flow Dynamics

As mentioned in Chap. 2, a benefit to modeling using TRUCHAS is its ability to handle multiphase flow systems. As such, detailed flow dynamics can be captured in both the air and water regimes, an advantage that many numerical models to date

are lacking. The applications associated with this capability are substantial, as little is known as to the flow in the air around a water wave attributed to the difficulty associated with studying such dynamics in a laboratory setting.

One laboratory study, outlined in Chap. 1, was dedicated solely to the investigation of air flow surrounding a wave. Through the use of a mercury-water model, Zagustin (1972) observed a circulation flow pattern above each breaking water wave. He reasoned that it was this flow pattern that was responsible for the transfer of energy from air to sea. Though rudimentary in design, and obviously using a fluid other than air, Zagustin (1972)'s investigation was the first look into the role of air flow in the complex interaction between air and sea.

Though not directly pertinent to the scope of this study, it is interesting to comment on the air flow pattern generated by TRUCHAS in relation to that explored by Zagustin (1972). Fig. 4–21 is a depiction of the air flow surrounding the wave of interest at the critical point in the numerical simulations. As is exemplified in this figure, TRUCHAS does indeed predict a circular flow behavior in the air surrounding the steep wave event. The ability of TRUCHAS to capture such flow details illustrates just one of the many diverse and robust capabilities of this model. The detailed flow dynamics that can be captured in the air by this model certainly warrant further scrutiny; a task, however, that is left for a future study.

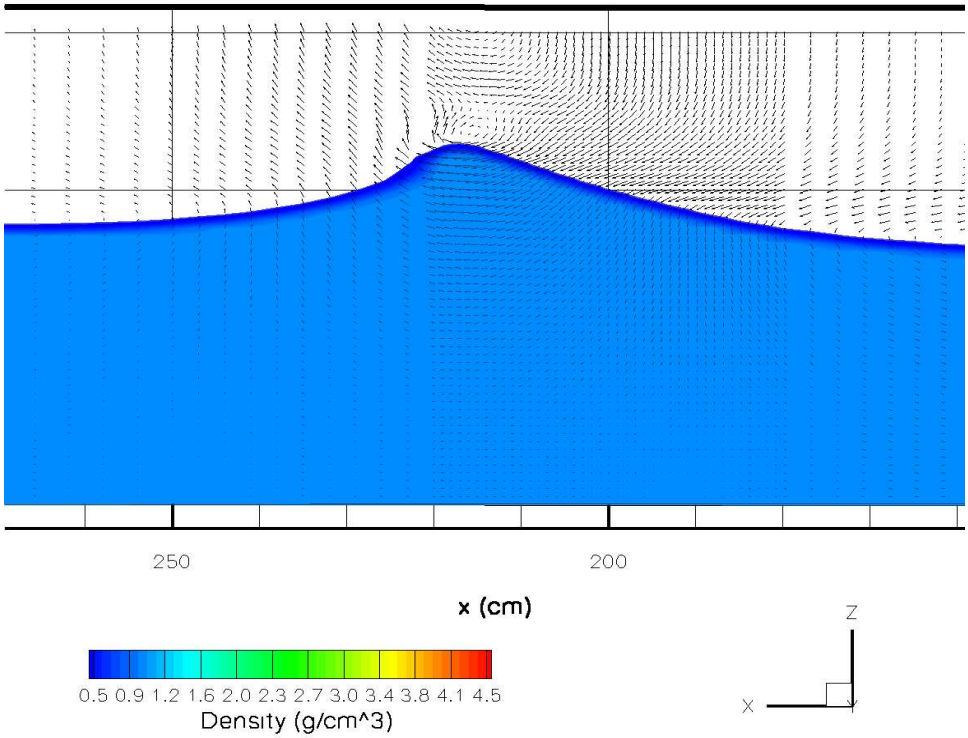

Figure 4–21: A depiction of the air flow pattern surrounding a water wave.

CHAPTER 5
DISCUSSION

5.1 Applications

The applications of a model as robust as TRUCHAS are endless. Numerous algorithms included within the the model's vast code allow for the numerical computation and simulation of such phenomena as heat transfer and phase changes, chemical reactions, solid mechanics, electromagnetics, and fluid dynamics. Manipulation of the basic user input files are straightforward, making the vast expanses of this code accessible to even the inexperienced modeler. Manipulation of the numerical algorithms themselves, however, provide a much more challenging task, as the model's numerous modules are intricately linked. Thus, even more experienced modelers may encounter challenges when trying to navigate or to adjust the innerworkings of TRUCHAS. Additionally, the complexity of this massive model comes at a computational cost, and the large simulation time required to resolve fine grid meshes may be discouraging to some modelers working on modest computational platforms.

Still, the virtues of a model such as TRUCHAS often outweigh the cost. Even within the fluid dynamics realm, this fully 3D model has a large range of capabilities. One distinct advantage of this model over many others is its ability to handle multiphase flow systems. Simple additions to the input files allow for the modeling of air, water, and/or any other material vital to the problem at hand. As such, with relatively little effort TRUCHAS would provide a good means by which to examine flow around structures, scour, or sediment transport problems.

Arguably the greatest attribute of this 3D model is that the user is provided with the capability to both control and accurately simulate the flow of air over the water surface. This feature is crucial in any investigation of air-sea interaction.

If left to its own devices, the model will simulate the air flow in response to any disturbances within the water column. Conversely, the user also has the option of forcing a specified air flow within the domain. Consequently, an in-depth numerical study of wind-generated waves may be accomplished; a detailed investigation which, to the authors' knowledge, has yet to be successfully undertaken. The wealth of knowledge that could be realized regarding such air-sea interactions as momentum and energy transfer across the interface from such an investigation is immense. It would seem, therefore, that this study has only scratched the surface of the many environmental investigations to which TRUCHAS can be applied.

5.2 Specifications

TRUCHAS relies heavily on user input to accurately depict flow conditions within a numerical simulation. Care must be taken to correctly specify material properties in this Navier-Stokes model. As there are no dimensional constants within TRUCHAS, save the gas constant, the user may specify any unit system to his liking. This requires, however, a careful review of all input variables, as fluid properties with differing unit systems will provide errors that are impossible to debug. Thus, the user holds much control over his numerical study, and must take great caution and responsibility in representing the natural phenomenon in question as completely as is possible.

The simplistic nature of the algebraic turbulence model included in such a robust and hearty 3D model is unfortunate. In fact, the Telluride Team, creators of TRUCHAS, cite this addition as a weak link in the code, and vow to update and improve upon the turbulence model in TRUCHAS versions to come. Application of the algebraic turbulence model to our study did little to improve the outcome of our simulations. Rather, turbulent fluctuations seemed to be more accurately captured when the algebraic model was not activated. Questions arise as to the correct mixing length that need be specified in order to accurately apply the algebraic turbulence scheme to a study such as the one conducted in this work. Hence, lack of a sound turbulence model

could be a hindrance to breaking wave studies using this version of TRUCHAS, and the implementation of a new turbulence model may allow future versions of this code to be more successful in endeavors similar to those attempted in this study.

The sensitivity of TRUCHAS to the cell aspect ratio is unfortunate, given the computational expense associated with powering such an involved model. The benefits of improved resolution, however, may prove invaluable in the accurate representation of turbulent structures and other breaking characteristics, and thus remains an important issue to be further addressed in the validity of TRUCHAS in its application to this realm of scientific exploration. Improvements made in the combination of numerical parameters employed in simulations, including courant number, convergence criterion, relaxation parameter, preconditioning steps, and maximum number of iterations, may save on computational time, thereby allowing for increased resolution at no added computational cost. Similarly, the modification of TRUCHAS to run in parallel will effectively remove the restriction on mesh resolution currently in place, as run times will see significant reductions. As is the case with any numerical model, TRUCHAS users would do well to recognize both the limitations as well as the plausible benefits associated with each specification opted for in any given numerical simulation.

5.3 Summary of Findings

The questions surrounding deep-water wave breaking events and their role in air-sea interaction are manifold. At present, a fully 3D model capable of precisely simulating all of the complex dynamics associated with this phenomenon remains to be developed. Such a numerical code could remain elusive for some time to come. Still, significant advances in the accurate numerical depiction of the air and sea during breaking events are being made continuously. It is our hope that this work may be one such step in the quest to understand one of the most common events we encounter in nature.

The objective of this investigation was to modify the flow dynamics of TRUCHAS to handle a focusing wave technique, and then to verify the ability of the model to accurately predict the resulting deep-water breaking wave events. Laboratory experiments conducted by Mark Donelan and Brian Haus at the University of Miami provided the means by which to force the model as well as to validate model predictions. Numerical forcing of a Gaussian wave packet was accomplished by implementing the free-surface elevation and orbital velocities obtained in the controlled laboratory setting. Focusing of the wave packet transpired, and the model's resulting η and u and w profiles could then be compared to laboratory results at a point downstream of the breaking region. Numerous computational runs were conducted in which specifications including surface tension models, turbulence models, and various cell aspect ratios were independently investigated. Final simulations were conducted with what was deemed the most comprehensive, yet computationally efficient scheme.

The results of this undertaking, though somewhat disappointing, gave great insight into the capabilities of this volume of fluid model. A qualitative analysis of the breaking region yielded no definitive evidence of a spilling event within the numerical simulations. Visual observations of the free-surface orientation computed during model runs did not indicate overturning or significant disruption of the fluid interface. Though mean velocity measurements were high in the crest of the wave of interest, total rms deviation from the mean velocity was small within this location, indicating little turbulence production that would have indicated breaking activity.

Both horizontal and vertical velocity components, as well as free-surface elevations, at location B demonstrated increased values in comparison to laboratory measurements. In addition, a phase lag of the laboratory data was seen to occur just after the passing of the critical wave crest. It is expected that turbulence produced by the spilling laboratory breaker would spawn eddies and act to hinder the advancement of the waveform, in accordance with the literature. This slowing of the breaking

wave could thus introduce the phase lag seen in the data. Similarly, the energy required to create the turbulence associated with breaking would come from the kinetic energy of the initial wave, thus accounting for diminished laboratory velocities in comparison to model data. The model wave, however, having not undergone a significant breaking event, did not experience these effects, and thus retained its higher velocity and free-surface values downstream of the breaking zone. As the secondary wave passed the plane of interest, however, there was a reversal in the data trends. The subsequent laboratory waves had ample opportunity to overtake the turbulent, slowly-propagating breaker. Thus, the velocities within these steepening waves were increased, corresponding with higher free-surface displacements. The wave also seemed to propagate faster in time as the phase lag experienced by the spilling breaker was not realized in the subsequent waves. Conversely, the secondary model waves never fully overtook the critical wave. As such, less steepening occurred and their velocities continued to diminish, thus producing what appears to be a phase lag in the model data in comparison to the laboratory profiles for the subsequent waves.

The results of the numerical investigation infer the failure of the focused wave packet to reproduce a spilling breaker at these grid resolutions. Instead, model results suggest a movement of the steep wave event away from breaking and toward a more stable configuration. The free-surface elevation profile at location B generated by TRUCHAS is noteworthy in its seemingly more uniform appearance. These results seem to indicate that nonlinearities within the flow dynamics trigger the steepened wave to devolve into a more stable, regular wave packet formation. In researching this phenomenon, it was discovered that other computational codes have experienced similar results. An investigation into the plausible explanations for such an occurrence is provided is the following section.

5.4 Recurrence

Although unfortunate, it does not appear that the failure of TRUCHAS to produce a spilling breaker is an uncommon problem. The nature of the evolution to breaking of deep-water waves has been an area of intense scrutiny for quite some time. Such investigations have led to well-documented instabilities known to develop within deep-water wave trains, producing nonlinear modulations. Benjamin and Feir (1967) were one of the first to document such instabilities, showing analytically that finite amplitude deep-water progressive waves are fundamentally unstable. Their findings, which have come to be known as the Benjamin-Feir Instability, illustrate that a periodic progressive wave with a fundamental frequency has also present residual wave motions at sideband frequencies that can increase exponentially as wave evolution progresses. The resulting waveform can become highly irregular far from its origin, and such wave trains will act to subside if given ample space. Laboratory investigations performed by Melville (1982) confirmed the Benjamin-Feir Instability to be present in experimental deep-water waves.

A second instability was discovered by Tanaka (1986) at the crest of regular waves. His investigation unearthed an instability at the wave steepness corresponding to the maximum total energy of the waveform. The Tanaka Instability, as it is now referred, occurs only at the steepest wave crests, and has been proven to be a local response to disturbances within the wave crest, thereby not being affected by the dynamics of the wave train in its entirety. An interesting conclusion drawn from this investigation, and most pertinent to our study, is that the evolution of the Tanaka Instability can lead to one of two plausible outcomes in the progression of the waveform. Though not well understood as to exactly why a wave will advance toward one extreme or the other, waveforms examined within the context of this study either progress on to breaking, or else undergo what is referred to as recurrence, whereby the wave demodulates back to close to its initial form, thus becoming more stable.

The discovery of these nonlinear modulations have provided some insight into the breaking and recurrence phenomenon experienced by many in the numerical investigations of wave breaking. Still, the underlying trigger that would cause such unstable waves to proceed toward either breaking or recurrence remains elusive and has spawned an intense examination into the nature of numerical breaking. Many attempts have been made to quantify in some universal constant the likelihood that a given steep wave event within a wave train will either undergo breaking or rather recurrence back to its initial signature. Banner and Tian (1998) performed an in-depth analysis of a periodic, 2D wave train to detail the onset of breaking or recurrence. The authors utilized a code constructed by Dold and Peregrine (1985) in which a Cauchy theorem boundary integral is used iteratively to solved Laplace's Equation through the evaluation of multiple time derivatives of the surface motion. Banner and Tian (1998) then added their own interior code to the model to compute the interior flow field from the free-surface orientation at every time during the simulation using a spectral method. Their investigation suggested that the onset of breaking or recurrence was dictated by the nonlinear behavior of the wave group, and could be determined by the relative growth rates of the mean momentum and energy densities. Findings indicated that breaking occurred when the mean momentum and energy growth rates surpassed a certain threshold value. In contrast, steep waves could be expected to undergo recurrence without breaking if these growth rates reach the threshold value and immediately began to decline.

Henderson *et al.* (1999), focusing mainly on the nonlinear modulation of 2D periodic wave trains over several thousand wave periods, observed similar results. Similar to Banner and Tian (1998), Henderson *et al.* (1999) also adopted the code of Dold and Peregrine (1985). Capable of simulating 2D flow fields up to overturning with a slight smoothing scheme, this model has been proven accurate in the simulation of uniform, irrotational, periodic wave trains. Henderson *et al.* (1999) did not include

an interior code. Rather, their focus was on the behavior of a deep-water wave train with varying initial steepnesses and the number of waves per train. The authors noted that energy becomes focused into a short group of steep waves, often that possess a wave steep enough to break. Occasionally, however, the wave group seems to reach a maximum modulation and then proceeds to demodulate, and recurrence transpires until an almost uniform wave train is recovered. A similar outcome seems to be suggested by the results of our study: Fig. 4–10, depicting free-surface displacement at location B, shows similar values for η at the crest of both the wave of interest, or the preliminary waveform in the plot, and the subsequent waveform. Although these waves are not periodic in nature, as those examined by Henderson *et al.* (1999), our model results seem to illustrate the tendency of a steep wave event having undergone recurrence to devolve into a nearly uniform, stable wave train.

Of particular interest to our investigation, Song and Banner (2002) conducted a study into the onset of breaking for deep-water wave trains of varying complexity. Among the wave trains simulated, the authors included a class of wave trains deemed "chirped" wave packets, in which a steep wave results from the focusing of a wave packet, very similar to the method used by Rapp and Melville (1990) in the laboratory, and analogous to the wave packets utilized in our study. The 2D numerical model employed by Song and Banner (2002) solves the fully nonlinear, irrotational free-surface boundary value problem with a boundary element method. A piston wavemaker is included at one end of the numerical domain, with an energy-absorbing beach at the other end. Initial conditions were that of a still water tank, and simulations were carried out past the point of overturning.

In their investigation, Song and Banner (2002) disproved the theory that instabilities within steep wave events are contingent upon the number of waves, N, within a wave packet, as had been suggested in previous studies. Instead, the authors' findings support those of Banner and Tian (1998), citing the average growth rate of

a dimensionless energy parameter to be the determining factor in the evolution of a water wave to recurrence or breaking. Within each class of wave trains studied, it was determined that a dimensionless growth rate threshold existed defining the breaking and recurrence regimes. Should the energy growth rate of the wave exceed this threshold, the wave was found to break. Conversely, if the maximum values of the energy growth rate remained below this threshold value, recurrence was undergone. Threshold values, however, varied significantly between wave train classes. Thus a unique, universal breaking threshold could not be ascertained.

Though there is still much to be uncovered as to the exact nonlinearities that trigger the energy growth rate of waves to reach threshold values, much has been learned about the instabilities undergone by deep-water wave trains. The fact that our study and those above all vary in the approach of the simulation, yet all experience the same recurrence phenomenon is indicative of a nonlinear problem not unique to TRUCHAS. The added 3D nonlinearities certain to exist in our model, in comparison with those discussed above, may only compound the conditions leading to recurrence in TRUCHAS. Though there is no conclusive evidence of yet as to the specific nonlinearities dictating the recurrence of our model waves, the studies mentioned above have provided the beginnings of an explanation into the complex dynamics observed in these simulations. As more studies are conducted into the vast and highly complex nonlinear nature of deep-water waves, it is hoped that conclusions will be drawn as to the details surrounding the onset of wave breaking. Surely to follow, then, will be a more thorough and precise illustration of the numerical attributes triggering each type of breaking response, and improvements can be made to more accurately model the desired breaking regime.

5.5 Concluding Remarks

Despite the inability of TRUCHAS, given the numerical specifications, to produce a spilling breaker, much was learned regarding the varied capabilities of this robust

model. It is not implied that the failure of this study to result in a definitive breaker is suggestive of a complete inability of the model to accurately simulate spilling events. Much to the contrary, simulations involving increased amplitude waves were conducted in which spilling breakers occurred early in the simulations. Unfortunately, these breaking episodes transpired within the propagation region of the numerical domain, and thus did not accurately simulate the laboratory experiment. As such, these cases were not presented in this work. It is the opinion of the authors that increased resolution may significantly improve the performance of the code, and may reveal flow characteristics, such as turbulent structures, that are not readily observable given the specifications set forth in this numerical investigation. Ongoing research involving TRUCHAS is currently being conducted to further validate the model's ability to accurately reproduce spilling events experienced in laboratory settings. Current simulations involve significant increases in grid resolution as well as the addition of a cross-tank perturbation in the horizontal velocity field. It is the authors' hope that such improvements will not only provide the instabilities needed to ensure a breaking event will occur, but also will allow for the simulation of small-scale turbulence and other breaking characteristics. Still, TRUCHAS has proven a worthy numerical tool in the investigation of air-sea interactions and is found to have capabilities certain to prove useful in future investigations into breaking events and wind-generated waves. The exploration into the advances that can be accomplished through the use of TRUCHAS is still young, and with the correct combination of resolution and user inputs, it is likely that TRUCHAS will be a valuable asset to the engineering world.

APPENDIX
WIND-GENERATED WAVES

The capabilities of a model such as TRUCHAS are manifold, and a magnitude of research can be conducted with such a tool. As mentioned briefly in Chap. 1, a discovery was made during this study suggesting the possibility that TRUCHAS can be used to simulate the development and evolution of wind-generated waves. Though outside of the scope of this study, a brief examination was conducted in an attempt to verify this hypothesis.

A simple orthogonal mesh was generated spanning 1 m in length, 0.5 m in width, and 0.6 m in height. Grid resolution remained fairly coarse to allow for faster convergence. The corresponding cell aspect ratio, $\delta x : \delta y : \delta z$, was 4:5:2. The mean water level for the given scenario was 30 cm, with free-slip boundary conditions on the sidewalls and along the closed top of the tank. Above the mean water level, a constant-pressure, open boundary condition was enforced at the endwall to allow the unobstructed flow of air out of the numerical tank. A 7 m/s (approximately 15.7 mph) wind was then blown over the water body, which was initially at rest. The model was permitted to run for a short 3 second time span and qualitative results were documented.

Fig. A–1 shows two time shots of the simulation. Plot A), taken at time 0.48 seconds, depicts the initial formation of wind-generated waves caused by the shear stress imparted on the initially still water column by the movement of the air. A more fully-developed wave field has evolved by the second time shot, B), taken at 2.61 seconds into the simulation. In addition, interesting flow dynamics appear to be happening at the inflow boundary, with the possibility of air entrapment beneath the water surface at this location. Without argument, a more detailed investigation of this

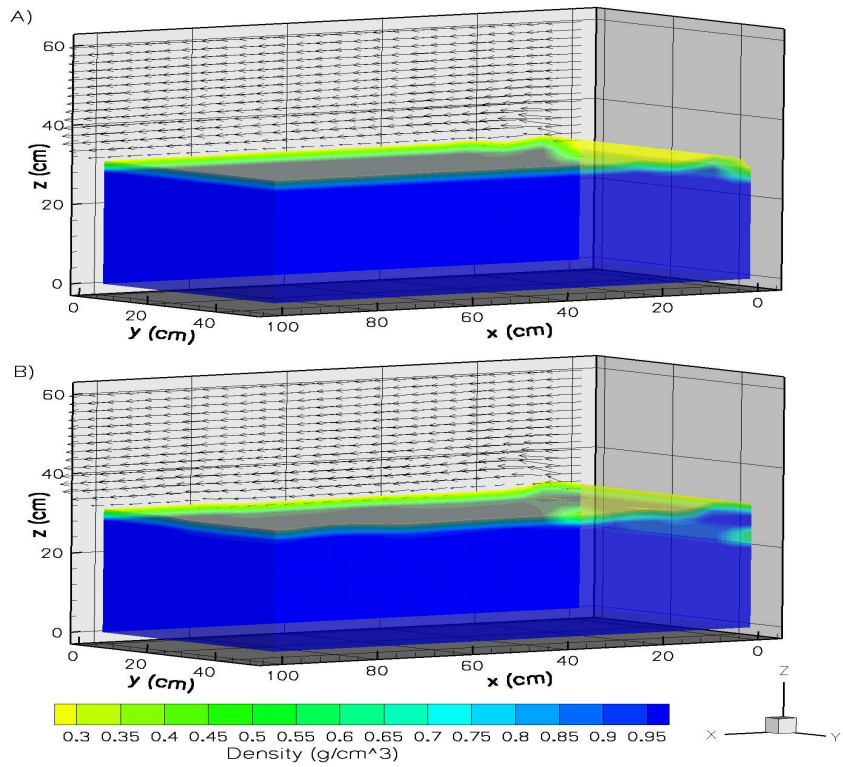

Figure A–1: Snapshots of waves generated by a 7 m/s wind across a water body initially at rest. Initial wave generation, at 0.48s, is shown in A), while a depiction of a more fully-developed wave field, at 2.61s, is presented in B).

scenario, requiring a more finely-resolved mesh and improved boundary conditions, is needed to quantitatively give sound evidence of the phenomenon in question.

To our knowledge, a fully 3D numerical study has yet to be conducted illustrating flow dynamics in both the air and sea associated with the complicated development of wind-generated waves. Most numerical models, to this point, are unable to fully resolve the velocities in both fluids and are either idealized, or focus entirely on the dynamics of the water column. It would seem that, though this study was brief and rudimentary at best, our findings warrant a closer look into the capabilities of this vast model.

REFERENCES

BANNER, M. L. & PEREGRINE, D. H. 1993 Wave breaking in deep water. *Annu. Rev. Fluid Mech.* **25**, 373–397. 1.2

BANNER, M. L. & TIAN, X. 1998 On the determination of the onset of breaking for modulating surface gravity water waves. *J. Fluid Mech.* **367**, 107–137. 1.2, 5.4

BENJAMIN, T. B. & FEIR, J. E. 1967 The disintegration of wave trains on deep water. *J. Fluid Mech.* **27**, 417–427. 5.4

CHEN, G., KHARIF, C., ZALESKI, S. & LI, J. 1999 Two-dimensional Navier-Stokes simulation of breaking waves. *Phys. of Fluids* **11**, 121–133. 1.2

CHU, V. H. & MEI, C. C. 1971 The non-linear evolution of Stokes waves in deep water. *J. Fluid Mech.* **47**, 337–351. 1.2

CSANADY, G. T. 2001 *Air-Sea Interaction: Laws and Mechanisms*. Cambridge University Press, New York, New York. 1.2

DEAN, R. G. & DALRYMPLE, R. A. 1991 *Water Wave Mechanics for Engineers and Scientists*. World Scientific, River Edge, New Jersey. 1.1, 2.5.1, 4.1.2, 4.2.3

DEAN, R. G. & DALRYMPLE, R. A. 2002 *Coastal Processes with Engineering Applications*. Cambridge University Press, New York, New York. 4

DOLD, J. W. & PEREGRINE, D. H. 1985 *Numerical Methods for Fluid Dynamics II*, chap. An Efficient Boundary-Integral Method for Steep Unsteady Water Waves, pp. 671–679. Oxford University Press. 5.4

DOMMERMUTH, D. G., YUE, D. K. P., LIN, W. M., RAPP, R. J., CHAN, E. S. & MELVILLE, W. K. 1988 Deep-water plunging breakers: A comparison between potential theory and experiments. *J. Fluid Mech.* **189**, 423–442. 1.2

DONELAN, M. A., ANCTIL, F. & DOERING, J. C. 1992 A simple method for calculating the velocity field beneath irregular waves. *Coastal Eng.* **16**, 399–424. 1.2, 3.1, 3.2.2, 3.2.2, 4.2.1

DUNCAN, J. H. 2001 Spilling breakers. *Annu. Rev. Fluid Mech.* **33**, 519–547. 1.2

FLETCHER, C. A. J. 1991 *Computational Techniques for Fluid Dynamics*. Springer, Heidelberg, Germany. 2.4.4, 2.4.4

GRILLI, S. T., GUYENNE, P. & DIAS, F. 2001 A fully non-linear model for three-dimensional overturning waves over an arbitrary bottom. *J. Numer. Meth. Fluids* **35**, 829–867. 1.2

HENDERSON, K. L., PEREGRINE, D. H. & DOLD, J. W. 1999 Unsteady water wave modulations: Fully nonlinear solutions and comparison with the nonlinear Schrödinger equation. *Wave Motion* **29**, 341–361. 1.2, 5.4

HOLTHUIJSEN, L. H. & HERBERS, T. H. C. 1986 Statistics of breaking waves observed as whitecaps in the open sea. *J. Phys. Oceanography* **16**, 290–297. 1.2

KJELDSEN, S. P. & MYRHAUG, D. 1980 Wave-wave interactions, current-wave interactions and resulting extreme waves and breaking waves. In *Proc. 17th Conf. Coastal Eng.*, pp. 2277–2303. ASCE, Sydney, Australia. 1.2

KOTHE, D. B., MJOLSNESS, R. C. & TORREY, M. D. 1991 *RIPPLE: A Computer Program for Incompressible Flows with Free Surfaces*, LA-12007-MS edn. Los Alamos National Laboratory, University of California, Dept. of Energy. 2.1

KWAY, J. H. L., LOH, Y.-S. & CHAN, E.-S. 1998 Laboratory study of deep-water breaking waves. *Ocean Eng.* **25**, 657–676. 1.2

LIN, P. & LIU, P. L. F. 1999 Internal wave-maker for Navier-Stokes equations models. *J. Waterway, Port, Coastal, and Ocean Eng.* **125**, 207–215. 1.2

LIU, P. L. F. & LIN, P. 1997 *A Numerical Model for Breaking Waves: The Volume of Fluid Method, Tech. Rep.* Cornell University, Newark, New Jersey. 1.2

LONGUET-HIGGINS, M. S. 1978 *Turbulent Fluxes Through the Sea Surface, Wave Dynamics and Prediction*, chap. On the Dynamics of Steep Gravity Waves in Deep Water, pp. 199–220. Plenum Publishing Corp. 1.2

LONGUET-HIGGINS, M. S. & COKELET, E. D. 1976 The deformation of steep surface waves on water, Part I: A numerical method of computation. *Proc. R. Soc. Lond. A* **350**, 1–26. 1.2

LYONS, L. 1991 *A Practical Guide to Data Analysis for Physical Science Students*. Cambridge University Press, New York, New York. 3.3.3

MELVILLE, W. K. 1982 The instability and breaking of deep-water waves. *J. Fluid Mech.* **115**, 165–185. 5.4

MELVILLE, W. K. 1996 The role of surface-wave breaking in air-sea interaction. *Annu. Rev. Fluid Mech.* **28**, 279–321. 1.2

MELVILLE, W. K., VERON, F. & WHITE, C. J. 2002 The velocity field under breaking waves: Coherent structures and turbulence. *J. Fluid Mech.* **454**, 203–233. 1.2, 1

MIYATA, H. 1986 Finite-difference simulation of breaking waves. *J. Comp. Phys.* **65**, 179–214. 1.2

MUNSON, B. R., YOUNG, D. F. & OKIISHI, T. H. 2002 *Fundamentals of Fluid Mechanics*. John Wiley and Sons, Inc., Hoboken, New Jersey. 3, 5

PEYRET, R. & TAYLOR, T. D. 1985 *Computational Methods for Fluid Flow*. Springer-Verlag, New York, New York. 2.4.4

POPE, S. B. 2000 *Turbulent Flows*. Cambridge University Press, New York, New York. 4.1.3, 5, 6

RAPP, R. J. & MELVILLE, W. K. 1990 Laboratory measurements of deep-water breaking waves. *Phil. Trans. R. Soc. Lond. A* **331**, 735–800. 1.2, 3.1, 5.4

SONG, C. & SIRVIENTE, A. I. 2004 A numerical study of breaking waves. *Phys. of Fluids* **16**, 2649–2667. 1.2

SONG, J.-B. & BANNER, M. L. 2002 On determining the onset and strength of breaking for deep water waves, Part I: Unforced irrotational wave groups. *J. Phys. Oceanography* **32**, 2541–2558. 1.2, 5.4

TANAKA, M. 1986 The stability of steep gravity waves. *J. Fluid Mech.* **156**, 281–289. 5.4

TEAM, T. T. 2004 *TRUCHAS, Version 2.0*, LA-UR-03-9109 edn. Los Alamos Scientific Laboratory of the University of California. 2.1, 2.2, 2.3, 2.3, 2.4.1, 2.4.2, 2.4.3, 2.4.5

TULIN, M. P. & WASEDA, T. 1999 Laboratory observations of wave group evolution, including breaking effects. *J. Fluid Mech.* **378**, 197–232. 1.2

VANDORN, W. G. & PAZAN, S. E. 1975 *Laboratory Investigation of Wave Breaking, Part II: Deep Water Waves, Tech. Rep*. Scripts Inst. of Oceanography, San Diego, California. 1.2

VIAUSSER, B., GRILLI, S. T. & FRAUNIÉ, P. 2003 Numerical simulations of three-dimensional wave breaking by coupling of a vof method and a boundary element method. In *Proc. 13th Inter. Offshore and Polar Eng. Conf.*, pp. 333–339. Inter. Soc. of Offshore and Polar Eng., Honolulu, Hawaii. 1.2

XUE, M., XÜ, H., LIU, Y. & YUE, D. K. P. 2001 Computations of fully nonlinear three-dimensional wave-wave and wave-body interactions, Part I: Dynamics of steep three-dimensional waves. *J. Fluid Mech.* **438**, 11–39. 1.2

YUEN, H. C. & LAKE, B. M. 1980 Instabilities of waves on deep water. *Annu. Rev. Fluid Mech.* **12**, 303–334. 1.2

ZAGUSTIN, K. 1972 Energy transfer mechanism for finite amplitude waves. In *Proc. 13th Conf. Coastal Eng.*, pp. 523–536. Vancouver, B.C., Canada. 1.2, 4.4

BIOGRAPHICAL SKETCH

I spent my childhood in the small town of North Billerica, Massachusetts, just a short ride from Boston. I have many fond memories of the wonderful times that I spent with close friends and a tightly-knit family during those years, many of which involve the water. I was splashing in our in-ground pool before I had ever considered taking a step, and not a summer day went by that my brothers and I were not inventing new pool games or learning to water ski, tube, wakeboard, and boat at our lakeside cabin in Maine. I knew by the time that I was entering grade school that I would never be happy answering phones or typing memos for a living; I was meant to be on the sea.

It was on our first big family trip to Florida when I was in 5th grade that I pinpointed exactly what I was going to do with my life: I was going to train the dolphins at Sea World. I held onto that dream throughout the remainder of my time in Billerica. Upon graduating from Billerica Memorial High School in 1999, I set out to become a marine biologist. My dream took me to St. Petersburg, Florida, where I made one of the greatest decisions of my life to attend Eckerd College. The small, intimate setting at Eckerd was exactly what I needed during my first extended period of time away from my family. Small class sizes, multiple laboratory studies, and the school's on-site research vessels and waterfront property made the study of marine science both exciting and very accessible.

I soon learned, however, that there was much more under the surface of the ocean than simply marine mammals. After taking my first marine invertebrate class (and realizing the extent to which I would have to study such "critters," as we liked to refer to them, before I would eventually get to the good stuff, or the mammals), I began to seriously question my choice in concentrations. It was at that time that I

took my first marine geology class, and I immediately fell in love. By my sophomore year, I had decided to shift my focus to marine geophysics and went to work for Dr. Gregg Brooks, my marine geology professor and a sedimentologist. The experience I gained from that research assistantship, both in the laboratory as well as in the field, has been invaluable. During this time, I spent summers onboard research cruises collecting underway sediment samples, sidescan and seismic sonar data, and sediment cores. I also obtained my SCUBA certification, and had the amazing opportunities to study geology and volcanology abroad, in both Ecuador and the Galapagos Islands as well as in Tanzania, East Africa. I continue to be amazed at the opportunities made available to me at Eckerd College, and I am unbelievably happy to have made such an astounding choice in schools.

It was during a senior research study at Eckerd College that I worked with Dr. David Duncan, of both Eckerd College and the University of South Florida, in the collection of seismic (CHIRP) data. During this time, I learned how to collect and to analyze CHIRP data, and I presented a poster at the Gulf of Mexico Estuaries Integrated Science: Tampa Bay Pilot Study 2002 Poster Series in which I correlated CHIRP data with sediment cores taken in Safety Harbor, Tampa Bay. Having become extremely interested in seismic sonar studies, I began to think that a graduate program in coastal or oceanographic engineering might be an interesting supplement to my undergraduate experience. Thus, upon completion of my Bachelor of Science degree in marine science, with a concentration in marine geophysics and a minor in mathematics, in May of 2003, I enrolled in the University of Florida's coastal engineering program.

I was drawn to the University of Florida by a wonderful offer from Dr. Don Slinn to become a research assistant. Though sometimes difficult and somewhat frustrating, I have been very grateful for the experiences that I have had in the Civil and Coastal Engineering Department. Not only have I met some wonderful people and made some lifelong friends, but I have had many educational experiences that I never would have

imagined I would be involved in just a few short years ago. I have learned another side to scientific research, the world of computer modeling. Though this field is not necessarily where I feel most at home, my acquired skills in CFD have given me another tool to use in my research and have made me a more diverse and skilled scientist and engineer. Combined with my undergraduate experiences, my time spent in the Civil and Coastal Engineering Graduate Program at the University of Florida has made me more capable and confident in my scientific endeavors, and has provided me with the knowledge and experience I need to embark on an exciting career on, in, and around the ocean.